Genomically Mined Acoustic Reporter Genes Enable On-Demand *In Vivo* Monitoring of Tumor-Homing Bacteria

Robert C. Hurt[1,#], Marjorie T. Buss[2,#], Katie Wong[2], Daniel P. Sawyer[1], Margaret B. Swift[2], Przemysław Dutka[1,2], David R. Mittelstein[3], Zhiyang Jin[3], Mohamad H. Abedi[1], Ramya Deshpande[2], Mikhail G. Shapiro[2,*]

[1]Division of Biology and Biological Engineering, California Institute of Technology, Pasadena, CA, USA
[2]Division of Chemistry and Chemical Engineering, California Institute of Technology, Pasadena, CA, USA
[3]Division of Engineering and Applied Sciences, California Institute of Technology, Pasadena, CA, USA
[#]Equal contribution
[*]Correspondence should be addressed to M.G.S. (mikhail@caltech.edu)

ABSTRACT

A major outstanding challenge in the fields of biological research, synthetic biology and cell-based medicine is the difficulty of visualizing the function of natural and engineered cells noninvasively inside opaque organisms. Ultrasound imaging has the potential to address this challenge as a widely available technique with a tissue penetration of several centimeters and a spatial resolution below 100 μm. Recently, the first genetically encoded reporter molecules were developed based on bacterial gas vesicles to link ultrasound signals to molecular and cellular function. However, the properties of these first-generation acoustic reporter genes (ARGs) resulted in limited sensitivity and specificity for imaging in the *in vivo* context. Here, we describe second-generation ARGs with greatly improved acoustic properties and expression characteristics. We identified these ARGs through a systematic phylogenetic screen of candidate gas vesicle gene clusters from diverse bacteria and archaea. The resulting constructs offer major qualitative and quantitative improvements, including the ability to produce nonlinear ultrasound contrast to distinguish their signals from those of background tissues, and a reduced burden of expression in probiotic hosts. We demonstrate the utility of these next-generation ARGs by imaging the *in situ* gene expression of tumor-homing probiotic bacteria, revealing the unique spatial distribution of tumor colonization by these cells noninvasively in living subjects.

INTRODUCTION

Basic biological research, *in vivo* synthetic biology and the development of cell-based medicine require methods to visualize the function of specific cells deep inside intact organisms. Within this context, widely used optical techniques based on fluorescent and luminescent proteins have limited utility due to the scattering and absorption of light by tissue.[1] In contrast, ultrasound is a widely used technique for deep-tissue imaging, providing sub-100 μm spatial resolution at a depth of several cm (ref. [2]). The relative simplicity and low cost of ultrasound make it widely accessible for both research and clinical medicine. Recently, the first genetically encodable reporters for ultrasound were introduced based on gas vesicles (GVs),[3] air-filled protein nanostructures encoded by clusters of 8-20+ genes, which evolved as flotation devices in a wide range of mostly aquatic bacteria and archaea.[4,5] The low density and high compressibility of their air-filled interiors compared to surrounding tissues allow GVs to scatter sound waves and thereby produce ultrasound contrast when heterologously expressed as acoustic reporter genes (ARGs) in genetically engineered bacteria[6] or mammalian cells.[7]

Despite their promise, three major drawbacks have limited the utility of these first-generation ARGs in *in vivo* imaging. First, the GVs produced by existing ARGs scatter ultrasound linearly, making them difficult to distinguish from similar scattering by background tissues. Second, the existing bacterial ARGs express poorly at 37°C. Third, the formation of the resulting GVs is too burdensome for long-term expression. The first of these limitations is currently addressed by destructive ultrasound pulse sequences that irreversibly collapse GVs for signal subtraction, resulting in one-time contrast and limiting dynamic imaging. The second and third limitations have prevented the use of ARGs to image *in situ* gene expression by bacteria inside a mammalian host.[6]

To overcome these limitations, we sought next-generation ARGs that, when expressed heterologously in bacterial strains widely used as *in vivo* probiotic agents, produce GVs with strong nonlinear ultrasound contrast and enable strong, sustained expression under physiological conditions. These qualities would provide greatly improved utility for *in vivo* imaging. We hypothesized that a genomic mining approach – previously applied to improving fluorescent proteins, optogenetic receptors and other biotechnology tools[8–12] – would yield ARGs with improved properties, which could be further optimized through genetic engineering. By cloning and screening 15 distinct polycistronic operons from a diverse set of GV-expressing species representing a broad phylogeny, we identified a gene cluster from *Serratia sp.* 39006 that produces strong nonlinear acoustic contrast and enables high levels of low-burden GV expression in *E. coli*. Engineering an optimized expression system for this gene cluster in the widely used probiotic species *E. coli* Nissle 1917 (EcN) resulted in ARGs with sufficient performance to enable the noninvasive imaging of mouse tumor colonization and subsequent gene expression by these probiotic agents, providing direct visualization of a critical aspect of this rapidly emerging class of anti-cancer therapy.

RESULTS

Genomic mining of gas vesicle gene clusters reveals homologs with improved ultrasound performance in E. coli. GVs are encoded by polycistronic gene clusters comprising one or more copies of the primary structural gene

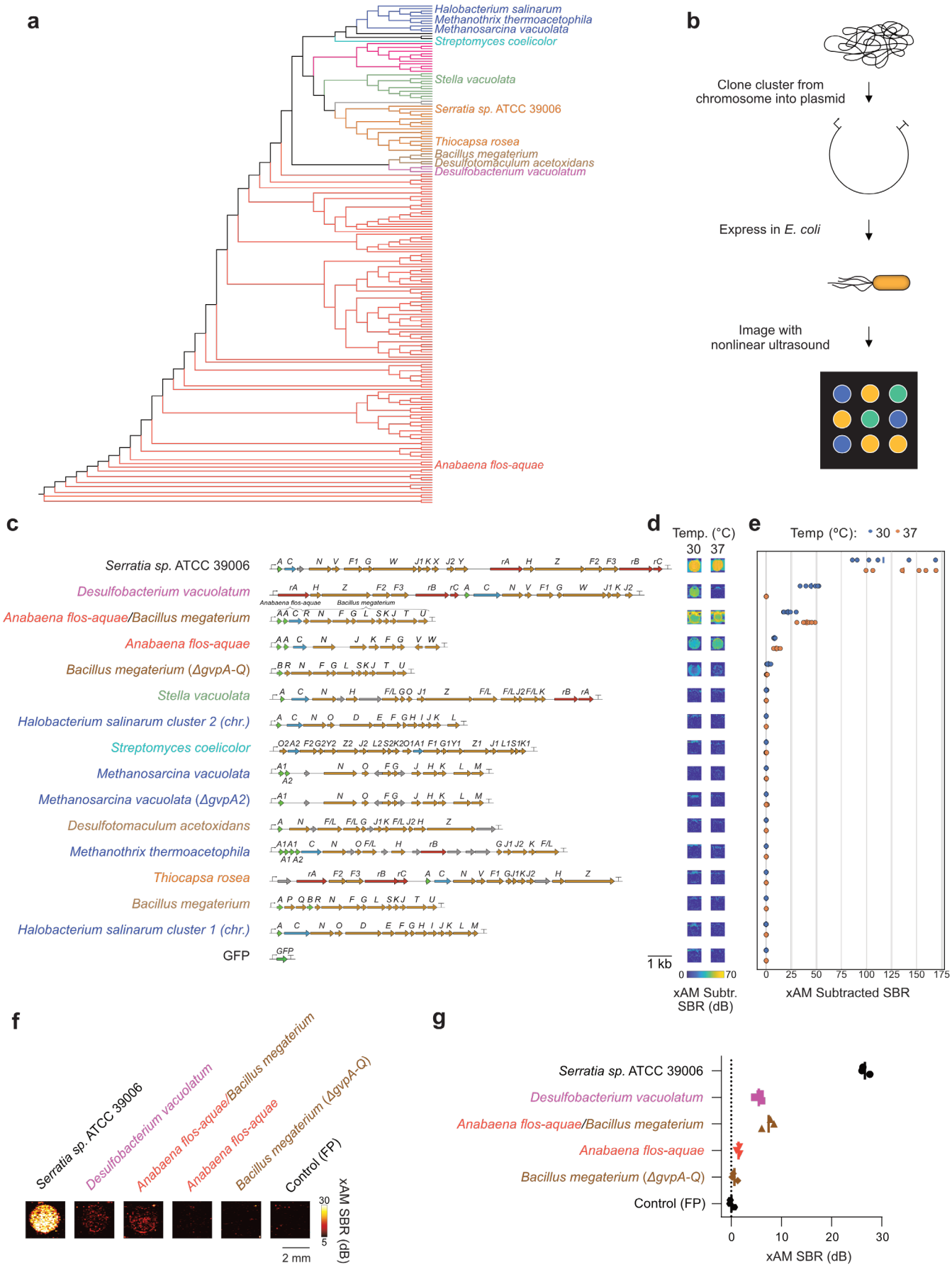
a
Halobacterium salinarum
Methanothrix thermoacetophila
Methanosarcina vacuolata
Streptomyces coelicolor
Stella vacuolata
Serratia sp. ATCC 39006
Thiocapsa rosea
Bacillus megaterium
Desulfotomaculum acetoxidans
Desulfobacterium vacuolatum
Anabaena flos-aquae
b
Clone cluster from chromosome into plasmid
Express in E. coli
Image with nonlinear ultrasound
c
Serratia sp. ATCC 39006
Desulfobacterium vacuolatum
Anabaena flos-aquae/Bacillus megaterium
Anabaena flos-aquae
Bacillus megaterium (ΔgvpA-Q)
Stella vacuolata
Halobacterium salinarum cluster 2 (chr.)
Streptomyces coelicolor
Methanosarcina vacuolata
Methanosarcina vacuolata (ΔgvpA2)
Desulfotomaculum acetoxidans
Methanothrix thermoacetophila
Thiocapsa rosea
Bacillus megaterium
Halobacterium salinarum cluster 1 (chr.)
GFP
d
Temp. (°C)
30 37
1 kb
0 70
xAM Subtr. SBR (dB)
e
Temp (°C): 30 37
0 25 50 75 100 125 150 175
xAM Subtracted SBR
f
Serratia sp. ATCC 39006
Desulfobacterium vacuolatum
Anabaena flos-aquae/Bacillus megaterium
Anabaena flos-aquae
Bacillus megaterium (ΔgvpA-Q)
Control (FP)
30
5
xAM SBR (dB)
2 mm
g
Serratia sp. ATCC 39006
Desulfobacterium vacuolatum
Anabaena flos-aquae/Bacillus megaterium
Anabaena flos-aquae
Bacillus megaterium (ΔgvpA-Q)
Control (FP)
0 10 20 30
xAM SBR (dB)

Figure 1 | Genomic mining of gas vesicle gene clusters reveals homologs with nonlinear ultrasound contrast in *E. coli*. (**a**) 16S phylogenic tree of known GV-producing organisms, with the species from which GV genes were cloned and tested in this study indicated by name. See **Fig. S1** for the fully annotated phylogenic tree. *B. megaterium* and *S. coelicolor* were not reported to produce GVs, but we tested their GV gene clusters here based on previous experiments in *E. coli*[5] and to broadly sample the phylogenetic space. (**b**) Workflow for testing GV clusters. Select GV gene clusters were expressed in BL21(DE3) *E. coli* by growing patches of cells on plates containing the inducer IPTG, and the patches were then imaged with nonlinear ultrasound (xAM). (**c-e**) Diagrams of the GV gene clusters tested in *E. coli* (c), pre-minus-post-collapse xAM images of representative patches (d), and quantification of the pre-minus-post-collapse xAM signal-to-background ratio (SBR) of the patches (n=6 biological replicates) (e). (**f-g**) Representative xAM images (f) and quantification of the xAM SBR (n=3 biological replicates, each with 2 technical replicates) (g) for the top 5 GV-producing clusters expressed in *E. coli* at 30°C on solid media and normalized to 5 x 10^9 cells/mL in agarose phantoms, imaged at 1.74 MPa. See **Fig. S7a-b** for the ultrasound signal at varying acoustic pressures.

GvpA and 7 to 20+ other genes encoding minor constituents, assembly factors or reinforcing proteins, which together help assemble the GVs' protein shell. Hundreds of organisms have GV genes in their genomes, but only a small subset have been shown to produce GVs. Given the labor involved in cloning and testing polycistronic clusters, we limited our phylogenetic search to organisms with confirmed GV production. From a list of 253 unique GV-producing species and 288 unique strains in the literature (**Table S1**), 117 have had their GV operons sequenced. We created a phylogenetic tree based on the 16S rDNA sequences of these organisms (**Fig. 1a** and **S1**) and used it to select 11 species, broadly sampling phylogenetic space, cluster architecture and organismal characteristics (*i.e.*, halophilic, thermophilic and mesophilic). We obtained each species from culture repositories, amplified GV operons from their genomes, and cloned them into a bacterial expression vector.

We then expressed each operon in confluent *E. coli* patches at several temperatures and inducer concentrations (**Fig. 1b**), comparing them to two bacterial ARG constructs previously shown to work in *E. coli*[6] – bARG1 (*Anabaena flos-aquae/Bacillus megaterium* hybrid) and *Bacillus megaterium ΔgvpA-Q*, as well as the full *Bacillus megaterium* gene cluster (**Fig. 1c-g**, **S2a-e, S3a-c**, **S4-6**). We scanned these patches using a robot-translated ultrasound probe, applying a nonlinear ultrasound pulse sequence involving the transmission of cross-propagating waves for amplitude modulation (xAM).[13] This pulse sequence enhances signals specific to nonlinear contrast agents such as GVs while reducing background tissue scattering. In addition, we examined the optical opacity of the patches, which can be increased by GV expression.

Of the 15 gene clusters tested, only 3 showed significant xAM signal when expressed at 37°C, and 5 showed significant xAM signal at 30°C (**Fig. 1c-e**). Only 3 clusters produced opaque patches at 30°C, all of which also produced significant xAM signal at this temperature (**Fig. S2c and S5a-b**). Even though all operons tested are from organisms reported to produce GVs, only the *Anabaena flos-aquae*, *Bacillus megaterium ΔgvpA-Q*, bARG1, *Desulfobacterium vacuolatum*, and *Serratia sp.* 39006 (*Serratia*) clusters produced GVs in *E. coli*. Several other operons produced visible ultrasound contrast under certain conditions, which did not arise from GV expression but reflected an effect on patch morphology, likely due to cellular toxicity (**Fig. S3d**). The failure of most tested gene clusters to produce GVs in *E. coli* reflects the complexity of polycistronic heterologous expression, which requires each component to fold and function properly in a new host with a potentially different cytoplasmic environment, growth temperature and turgor pressure.[14,15] In addition, it is possible that some genes included in the clusters act as cis-regulators,[5,14,16-18] limiting expression absent a specific trans input, or that some additional genes are required beyond the annotated operons.

In patch format, the strongest acoustic performance was observed with the genes from *Serratia*, bARG1, *A. flos-aquae*, *B. megateriaum*, and *D. vacuolatum*. Because patch experiments do not control for the density of cells in each sample, we further compared the performance of these clusters in resuspended samples. Each operon was expressed on solid media at 30°C – a temperature at which all five operons produced GVs – then scraped, resuspended, and normalized for cell concentration. These samples were imaged in hydrogels using xAM (**Fig. 1f-g and S7a-b**) and observed optically with phase-contrast microscopy (PCM) (**Fig. S7c**). Three of the clusters produced xAM signals significantly stronger than the negative control, and all clusters except *A. flos-aquae* exhibited sufficient GV expression to produce contrast in PCM.

Cells expressing the *Serratia* cluster produced the strongest ultrasound signals, 19.2 dB above the next brightest cluster, bARG1, at an applied acoustic pressure of 1.74 MPa – an 83-fold gain in signal intensity (**Fig. 1f**). Additionally, PCM images (**Fig. S7c**) showed that cells expressing the *Serratia* cluster had the highest levels of GV expression, as also seen in whole-cell transmission electron microscopy (TEM) (**Fig. S7d**). Based on the large improvement in ultrasound contrast provided by the *Serratia* GV operon relative to bARG1 and the other gene clusters tested in our phylogenetic screen, we selected this operon for further optimization as a second-generation ARG.

Because overexpression of any protein imposes a finite metabolic demand on the host cell,[19-21] we reasoned that deletion of non-essential genes could improve GV expression from the *Serratia* cluster, and therefore the xAM signal. Previous work has shown that deletions of *gvpC, gvpW, gvpX, gvpY, gvpH*, or *gvpZ* preserve GV formation in the native organism.[14] We tested these deletions, as well as the deletion of an unannotated hypothetical protein (Ser39006_001280) encoded between the *gvpC* and *gvpN* coding sequences (**Fig. S8a**). When expressed in *E. coli*, deletions of *gvpC, gvpH, gvpW, gvpY,* or *gvpZ* reduced or eliminated xAM signal (**Fig. S8b-c**) and patch opacity (**Fig. S8d**). Deletion of *gvpX* increased xAM signal but decreased opacity, and deletion of Ser39006_001280 increased both xAM signal and opacity. Based on these results, we chose to use the *Serratia* ΔSer39006_001280 operon for subsequent *in vitro* and *in vivo* experiments. We call this genetic construct

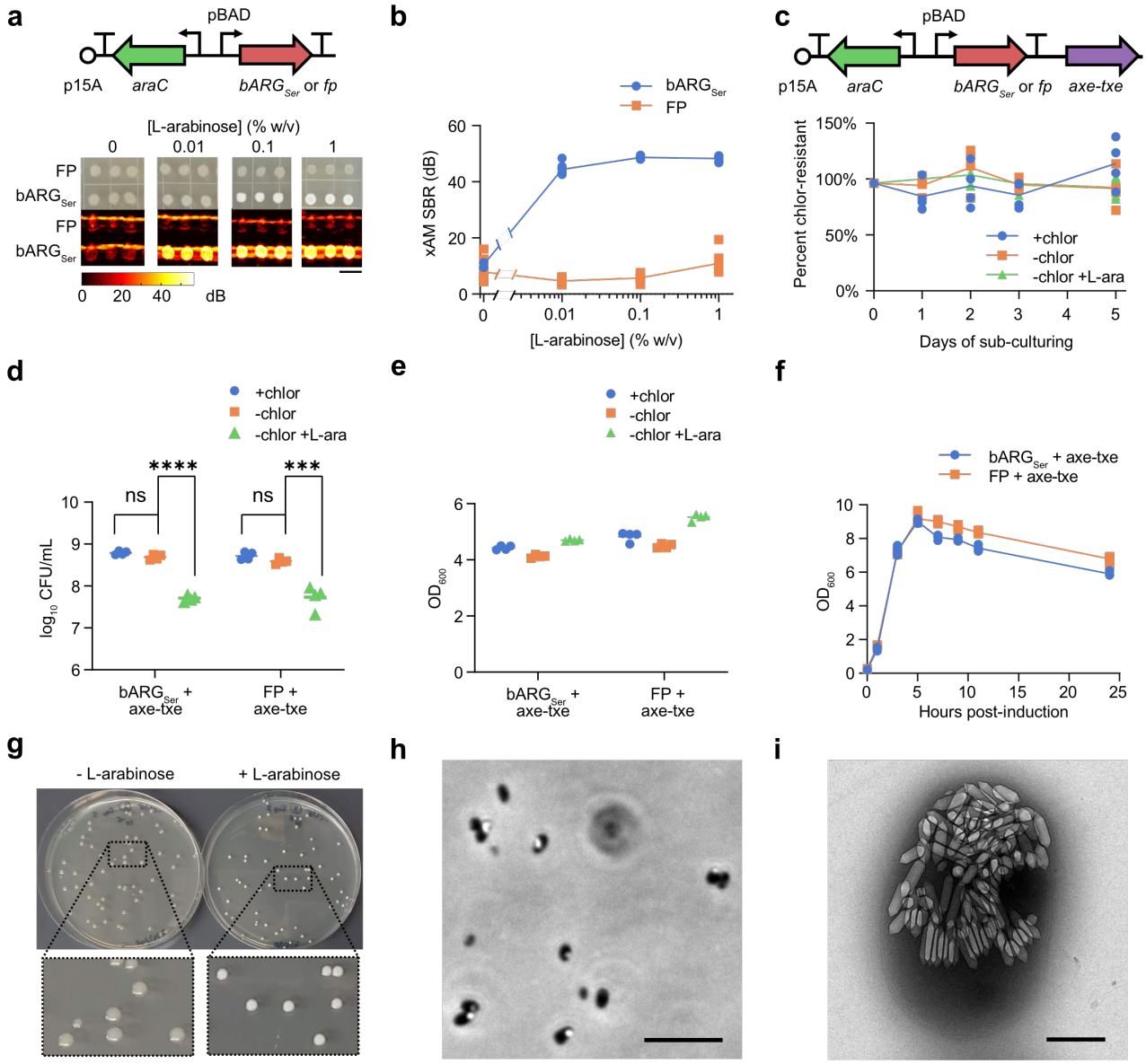

Figure 2 | Genetic engineering and expression of bARG$_{Ser}$ in the probiotic bacterium *E. coli* Nissle (EcN). **(a)** Diagram of the arabinose-inducible construct used to express bARG$_{Ser}$ in EcN (top), and optical and xAM images of bARG$_{Ser}$-expressing or FP-expressing patches of EcN on solid media with varying L-arabinose concentrations at 37°C (bottom). The scale bar is 1 cm. See **Fig. S9** for the corresponding results with IPTG-inducible and aTc-inducible constructs. **(b)** Quantification of the xAM SBR of all patches from the experiment in (a) versus the L-arabinose concentration (n=8 biological replicates). **(c)** Diagram of the construct from (a) with the toxin-antitoxin stability cassette Axe-Txe[29] added to enable plasmid maintenance in the absence of antibiotics (top), and verification of plasmid maintenance *in vitro* (bottom). The percentage of chloramphenicol-resistant colonies was measured during daily sub-culturing into LB media with 25 µg/mL chloramphenicol (+chlor), without chloramphenicol (-chlor), or without chloramphenicol and with 0.1% (w/v) L-arabinose (-chlor +L-ara) using pBAD-bARG$_{Ser}$-axetxe EcN (n=4 biological replicates). The percentage of chloramphenicol-resistant colonies was calculated by dividing the number of colonies on plates with chloramphenicol by the number of colonies on plates without chloramphenicol. **(d-e)** log10 of the colony forming units (CFUs) on chloramphenicol plates per mL of culture (d) and optical density at 600 nm (e) of pBAD-bARG$_{Ser}$-axetxe EcN and pBAD-FP-axetxe EcN cultures 24 hours after sub-culturing into LB media with the same conditions as in (c). Asterisks indicate statistical significance by unpaired t tests (**** = $p < 0.0001$, *** = $p < 0.001$, ns = no significance); n=4 biological replicates. **(f)** OD_{600} versus time after inducing pBAD-bARG$_{Ser}$-axetxe (bARG$_{Ser}$ + axe-txe) and pBAD-FP-axetxe (FP + axe-txe) EcN strains with 0.1% (w/v) L-arabinose in liquid culture at 37°C (n=4 biological replicates). Between 5 and 24 hours post-induction, when the OD_{600} of all cultures decreased, the OD_{600} of FP-expressing cultures was slightly higher than that of the bARG$_{Ser}$-expressing cultures, likely due to expression of red fluorescent protein which is known to absorb light at 600 nm.[42] **(g)** Representative image of colonies from the experiment in (c) on chloramphenicol plates with (right) and without (left) 0.1% (w/v) L-arabinose. The opacity of the colonies on plates with L-arabinose indicates bARG$_{Ser}$ expression and was used to screen for mutants deficient in bARG$_{Ser}$ expression (see **Fig. S11**). **(h-i)** Representative phase contrast microscopy (g) and transmission electron microscopy (h) images of pBAD-bARG$_{Ser}$-axetxe EcN cells grown on plates with 0.1% (w/v) L-arabinose at 37°C. Scale bars are 10 µm (g) and 500 nm (h).

$bARG_{Ser}$ as a bacterial acoustic reporter gene derived from *Serratia*.

$bARG_{Ser}$ shows robust expression, contrast, and stability in E. coli Nissle. We next transferred $bARG_{Ser}$ into a strain of *E. coli* used widely in *in vivo* biotechnology applications. We selected the probiotic strain EcN because of its ability to persist in the gastrointestinal tract and colonize tumors.[22-24] Recently, EcN has been intensely investigated as the chassis for anti-tumor therapy delivery.[25-28] We first tested different inducible expression constructs in EcN on solid media at 37°C, observing xAM ultrasound contrast and patch opacity as a function of inducer concentration. While the expression of $bARG_{Ser}$ from the T5-lac promoter and pTetR promoter was either leaky or toxic (**Fig. S9**), the pBAD promoter provided tight control over the formation of ultrasound contrast (**Fig. 2a**) without obvious toxicity (**Fig. 2b**). At 0.1% and 1% (w/v) L-arabinose, patches produced the strongest optical opacity and xAM signal. Based on these results, we selected the pBAD-$bARG_{Ser}$ EcN strain for subsequent experiments.

To ensure that the pBAD-$bARG_{Ser}$ plasmid is maintained in the absence of antibiotic selection, as required in certain *in vivo* applications, we added the toxin-antitoxin stability cassette Axe-Txe.[29] This enabled the pBAD-$bARG_{Ser}$-axetxe plasmid to be maintained in EcN for up to 5 days of daily sub-culturing in liquid media without antibiotics, both with and without induction of ARG expression using 0.1% (w/v) L-arabinose (**Fig. 2c**).

The expression of most heterologous genes, including widely used reporter genes such as fluorescent proteins, results in some degree of metabolic burden on engineered cells.[20,21,30] Consistent with this expectation, the induction of pBAD-$bARG_{Ser}$ EcN with 0.1% (w/v) L-arabinose resulted in reduced colony formation to an extent similar to the expression of a fluorescent protein (FP) (**Fig. 2d and S10a**), even as the culture density measured by OD_{600} remained relatively unchanged (**Fig. 2e and S10b**). When the OD_{600} was measured after inducing cultures with L-arabinose, the growth curves of $bARG_{Ser}$-expressing and FP-expressing EcN were indistinguishable during the growth phase (0 to 5 hours), indicating that the two strains have similar growth rates (**Fig. 2f**). Collectively, these results suggest that overexpression of $bARG_{Ser}$ using the pBAD expression system in EcN is not significantly more burdensome than that of FPs, which are widely accepted as relatively non-perturbative indicators of cellular function.

To further examine the genetic stability of $bARG_{Ser}$ constructs, we plated cells from daily sub-cultures onto agar with 0.1% (w/v) L-arabinose and examined colony opacity (**Fig. 2g**) as a measure of retained GV expression. Of a total of 3824 colonies, nearly all were opaque (**Fig. 2g**), with GV expression confirmed by PCM and TEM (**Fig. 2h-i**). Only 11 colonies (<0.3% after ~35 cell generations) exhibited a reduction in opacity and were instead grey in appearance (**Fig. S11a**), representing a mutated phenotype confirmed by growing these cells on fresh media (**Fig. S11b**). PCM revealed that these rare grey mutants still produced GVs, but at lower levels than non-mutants. These results indicate that mutational escape from GV production is not a major issue for pBAD-$bARG_{Ser}$-axetxe EcN under typical conditions.

After establishing construct stability, we characterized the acoustic properties of $bARG_{Ser}$-expressing EcN. For cells induced with 0.1% (w/v) L-arabinose for 24 hours and suspended at 10^9 cells/mL in agarose phantoms, an xAM signal was detected at pressures above 0.72 MPa, rising with increasing acoustic pressure up to the maximum tested pressure of 1.74 MPa (**Fig. 3a**). To characterize the physical stability of GVs in these cells during ultrasound exposure, we measured the xAM signal over time at a series of increasing acoustic pressures (**Fig. 3b**). The xAM signal was steady at pressures up to 0.96 Mpa, at which point we observed a slow decrease in the xAM SBR, indicating that some of the GVs slowly collapsed despite sustained high xAM signals. We also imaged the cells with parabolic pulses, which can transmit higher pressures than xAM, and thus can be helpful *in vivo* to compensate for attenuation at tissue interfaces. When imaged with parabolic B-mode at varying acoustic pressures, the GVs started to collapse slowly at 1.02 MPa and more rapidly at 1.33 MPa and above (**Fig. 3c**). Based on these results, an acoustic pressure of 1.29 MPa was selected for xAM imaging and 1.02 MPa was chosen for parabolic AM (pAM) imaging in subsequent experiments to obtain the strongest signals while minimizing GV collapse.

Next, to characterize the dynamics and inducibility of $bARG_{Ser}$ in EcN, as well as the detection limit of $bARG_{Ser}$-expressing EcN with ultrasound, we measured xAM signal as a function of induction time, inducer concentration, and cell concentration. Imaged at a density of 10^9 cells/mL, xAM signal could first be observed 7 hours after induction with 0.1% (w/v) L-arabinose in liquid culture and leveled off by 9 hours post-induction (**Fig. 3d-e**). Keeping the induction time constant at 24 hours while varying the L-arabinose concentration, GV expression was detected with as little as 0.001% (w/v) L-arabinose, and the highest ultrasound signal was observed for 0.1-1% (w/v) L-arabinose (**Fig. 3f-g**). When cells induced for 24 hours with 0.1% (w/v) L-arabinose were diluted, they were detectable by ultrasound down to 10^7 cells/mL (**Fig. 3h-i**). Critically, this detection was achieved non-destructively with nonlinear imaging, compared to previous bacterial ARGs, which required a destructive linear approach and made it difficult to distinguish ARG signal from that of background tissue. The $bARG_{Ser}$ xAM signal was proportional to the cell concentration between 10^7 cells/mL and 2 x 10^9 cells/mL (**Fig. 3h-i**). In sum, the reporter gene construct pBAD-$bARG_{Ser}$-axetxe is robust and stable in EcN, and enables gene expression in these cells to be imaged with high contrast and sensitivity.

$bARG_{Ser}$ enables in situ imaging of tumor-colonizing bacteria. Tumor-homing bacteria are a major emerging class of cancer therapy, which take advantage of the ability of cells such as EcN to infiltrate tumors and grow in their immunosuppressed microenvironment. Major synthetic biology efforts have been undertaken to turn tumor-homing EcN cells into effective therapies for solid tumors.[25-28] However, despite the promise of this technology and the importance of appropriate microscale

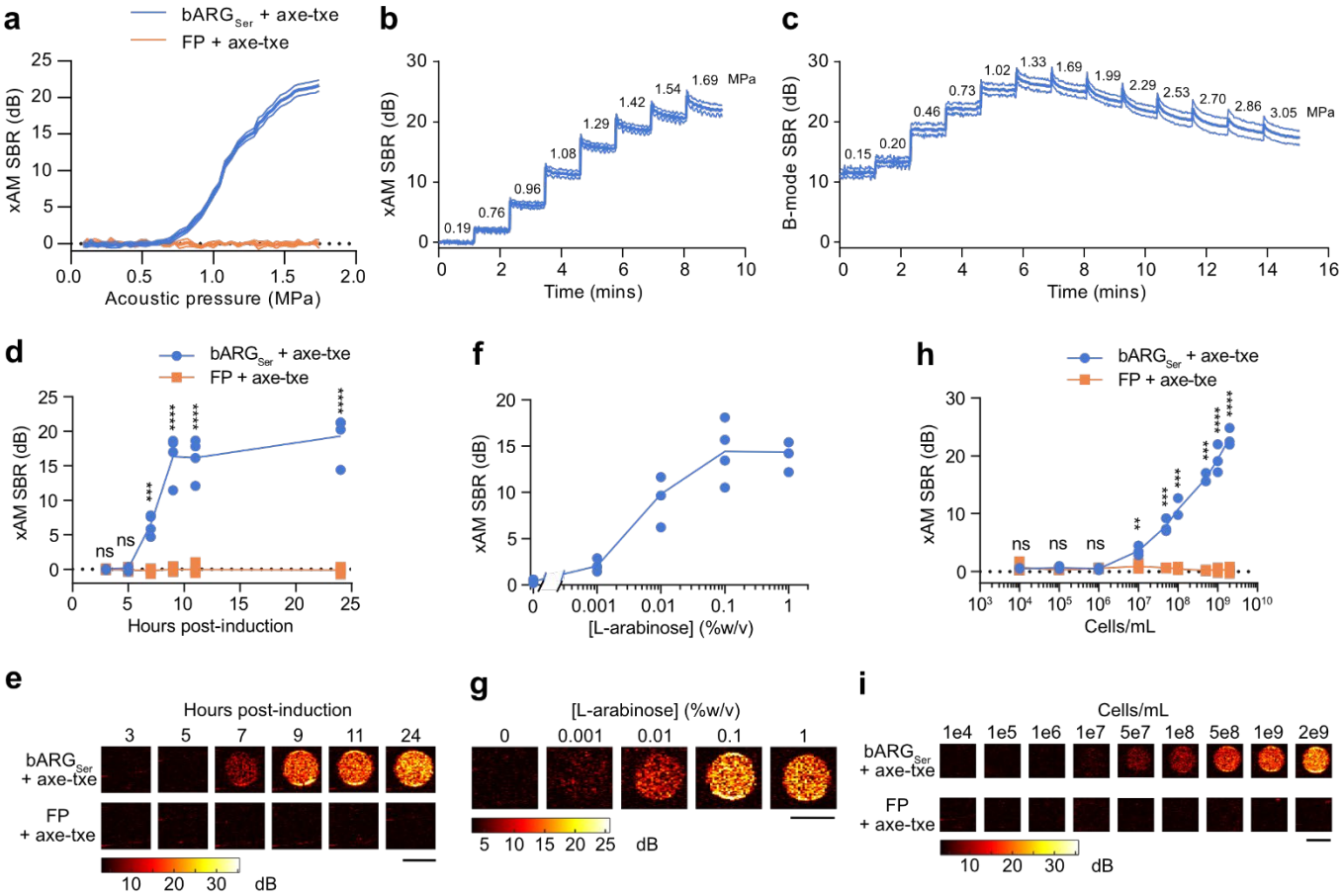

Figure 3 | Acoustic characterization of bARG$_{Ser}$-expressing EcN *in vitro*. (**a**) xAM SBR as a function of transmitted acoustic pressure for bARG$_{Ser}$-expressing and FP-expressing EcN. (**b-c**) xAM (b) and parabolic B-mode (c) SBRs measured over time when the transmitted acoustic pressure was increased approximately every 70 sec as indicated by the numbers above the curve for bARG$_{Ser}$-expressing EcN. Ultrasound was applied at a pulse repetition rate of 86.8 Hz. For (a-c), pBAD-bARG$_{Ser}$-axetxe EcN were induced with 0.1% (w/v) L-arabinose for 24 hours at 37°C in liquid culture, and were then normalized to 1 x 10^9 cells/mL in agarose phantoms for ultrasound imaging. Bold lines represent the mean and thin lines represent ± standard deviation; n=3 biological replicates, each with 2 technical replicates. (**d-e**) xAM ultrasound SBR (d) and corresponding representative ultrasound images (e) at several times after inducing pBAD-bARG$_{Ser}$-axetxe (bARG$_{Ser}$ + axe-txe) and pBAD-FP-axetxe (FP + axe-txe) EcN strains with 0.1% (w/v) L-arabinose in liquid culture at 37°C. (**f-g**) xAM ultrasound SBR (f) and corresponding representative ultrasound images (g) using varying L-arabinose concentrations to induce pBAD-bARG$_{Ser}$-axetxe EcN in liquid culture at 37°C for 24 hours. (**h-i**) xAM ultrasound SBR (h) and corresponding representative ultrasound images (i) of varying concentrations of pBAD-bARG$_{Ser}$-axetxe or pBAD-FP-axetxe EcN cells induced for 24 hours at 37°C with 0.1% (w/v) L-arabinose in liquid culture. For (e, g, i) scale bars are 2 mm. For (d-g), cells were normalized to 10^9 cells/mL in agarose phantoms for ultrasound imaging. For (d, f, h), each point is a biological replicate (n=4 for d and f; n=3 for h) that is the average of at least 2 technical replicates. Asterisks represent statistical significance by unpaired t tests (**** = p<0.0001, *** = p<0.001, ** = p<0.01, ns = no significance).

biodistribution of the bacteria inside tumors, no effective methods currently exist to visualize this biodistribution *in situ* in living animals.

To test the ability of bARG$_{Ser}$ to overcome this limitation, we formed MC26 tumors in mice and, when the tumors reached a substantial size, intravenously injected EcN containing the pBAD-bARG$_{Ser}$-axetxe plasmid, giving the bacteria 3 days to home to and colonize the tumors. We then induced GV expression and imaged the tumors with ultrasound (**Fig. 4a**). In all tumors colonized by bARG$_{Ser}$-expressing EcN, pAM and xAM ultrasound signals were observed 1 day after injection with L-arabinose (**Fig. 4b** and **S12a**). The signals were localized to the core of the tumor and concentrated at the interface between live and necrotic tissue,[23] where the EcN primarily colonized as confirmed with subsequent tissue histology (**Fig. 4f-h** and **S13**).

Furthermore, after collapsing all of the GVs by applying 3 MPa acoustic pressure throughout the tumor, re-injecting mice with L-arabinose to induce expression, and allowing at least 24 hours for re-expression, similar ultrasound signals were observed in all tumors colonized by bARG$_{Ser}$-expressing EcN (**Fig. 4c** and **S12b**). This result indicates that bARG$_{Ser}$ can be used to visualize gene expression at multiple timepoints. Absent L-arabinose induction, no ultrasound signals were observed from bARG$_{Ser}$-containing cells (**Fig. 4d** and **S12c**).

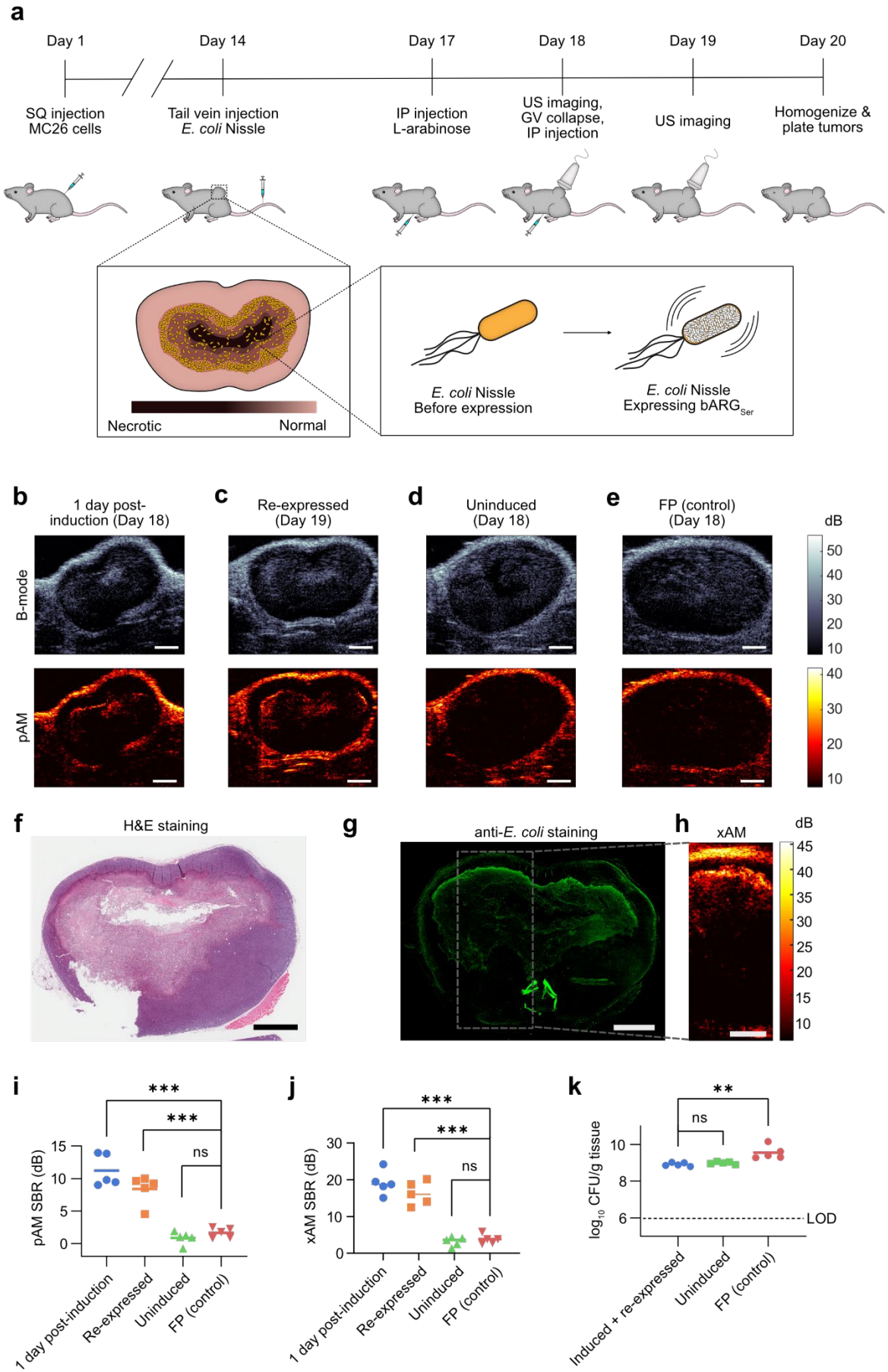
a
Day 1
Day 14
Day 17
Day 18
Day 19
Day 20
SQ injection MC26 cells
Tail vein injection E. coli Nissle
IP injection L-arabinose
US imaging, GV collapse, IP injection
US imaging
Homogenize & plate tumors
Necrotic
Normal
E. coli Nissle Before expression
E. coli Nissle Expressing bARG$_{Ser}$
b
1 day post-induction (Day 18)
c
Re-expressed (Day 19)
d
Uninduced (Day 18)
e
FP (control) (Day 18)
dB
B-mode
pAM
f
H&E staining
g
anti-E. coli staining
h
xAM
i
pAM SBR (dB)
1 day post-induction
Re-expressed
Uninduced
FP (control)
j
xAM SBR (dB)
k
log$_{10}$ CFU/g tissue
LOD
Induced + re-expressed
ns
***
**

Figure 4 | *In situ* bARG$_{Ser}$ expression enables ultrasound imaging of tumor colonization by EcN. (**a**) Diagram of the *in vivo* protocol for assessing *in situ* bARG$_{Ser}$ expression in tumors. Mice were injected subcutaneously (SQ) with MC26 cancer cells on day 1 and the tumors were allowed to grow for 14 days. Mice were then injected with *E. coli* Nissle (EcN) carrying either pBAD-bARG$_{Ser}$-axetxe or pBAD-FP-axetxe plasmids via the tail vein. After allowing 3 days for the EcN to colonize the tumors, bARG$_{Ser}$ or FP expression was induced by injecting L-arabinose intraperitoneally (IP) on day 17. The next day, at least 24 hours after induction, tumors were imaged with ultrasound. Subsequently, all the GVs in the tumors were collapsed by applying maximum acoustic pressure (3.0 MPa) throughout the tumor. L-arabinose was then injected again to re-induce bARG$_{Ser}$ expression, and tumors were again imaged with ultrasound at least 24 hours later. The next day (day 20), all mice were sacrificed, and their tumors were homogenized and plated on selective media to quantify the levels of EcN colonization. In separate experiments for histological analysis, mice were sacrificed on day 18 directly after ultrasound imaging. (**b-d**) Representative B-mode and parabolic AM (pAM) ultrasound images of tumors colonized by pBAD-bARG$_{Ser}$-axetxe EcN at least 24 hours after induction with L-arabinose on day 18 (b), at least 24 hours after collapse and re-induction (day 19) (c), or uninduced on day 18 (d). (**e**) Representative B-mode and parabolic AM (pAM) ultrasound images of tumors colonized by pBAD-FP-axetxe EcN at least 24 hours after induction with L-arabinose on day 18. (**f-g**) Optical images of tissue sections stained with H&E (f) or anti-*E. coli* antibodies (g) from a tumor colonized by bARG$_{Ser}$-expresssing EcN after ultrasound imaging on day 19. (**h**) xAM ultrasound image of the same tumor as in (f-g), with the boxed region showing the approximate imaging region in the tissue section. Scale bars in (b-h) represent 2 mm. (**i-j**) Quantification of the pAM (i) and xAM (j) SBR for the same conditions in (b-e); each group is n=5 mice. (**k**) Log10 of the colony forming units (CFUs) per gram of tissue from tumors homogenized and plated on day 20. The dotted line indicates the limit of detection (LOD). Asterisks represent statistical significance by unpaired t tests (*** = $p<0.001$, ** = $p<0.01$, ns = no significance). See **Fig. S12** for representative xAM ultrasound images for the conditions in (b-d), and **Fig. S13** for more histological images of tissue sections from tumors colonized with pBAD-bARG$_{Ser}$-axetxe EcN.

Likewise, no ultrasound signals were seen in tumors colonized by FP-expressing EcN (**Fig. 4e,i-j** and **S12d**).

To corroborate our ultrasound images of tumor colonization, at the end of the experiment all mice were euthanized at the same time point (day 20 in **Fig. 4a**) and their tumors were homogenized and plated on selective media. Tumors from all groups of mice (n=5 for induced + re-expressed bARG$_{Ser}$, n=5 for uninduced bARG$_{Ser}$, and n=5 for FP) contained more than 7 x 10^8 CFU/g tissue (**Fig. 4k**), indicating that the EcN can persist at high levels in tumors for at least 6 days after IV injection regardless of bARG$_{Ser}$ expression, collapse, and re-expression. The somewhat higher density of FP-expressing EcN suggested that maintenance of the smaller pBAD-FP-axetxe plasmid (7.2 kb versus 23.2 kb for pBAD-bARG$_{Ser}$-axetxe) may be easier in this *in vivo* context.

To test if there were any mutations causing a reduction or loss of the ability of the cells to produce GVs, tumors were plated on selective media with 0.1% (w/v) L-arabinose and screened for a reduction or loss of colony opacity (**Fig. S14a**). Out of a total of 6,097 colonies screened from ten mice, only seven colonies were not opaque (**Fig. S14b-c**), suggesting a low level of mutational escape. These results suggest that bARG$_{Ser}$ expression enables stable, high-resolution acoustic visualization of EcN in a clinically-relevant context without unacceptable burden.

DISCUSSION

Our results establish a new second-generation ARG construct, bARG$_{Ser}$, that provides unprecedented US detection sensitivity and specificity when expressed in probiotic *E. coli*. The cluster, selected through a systematic phylogenetic screen and optimized through genetic engineering, produces bright nonlinear US signal[13] when expressed *in situ* by bacterial agents colonizing the necrotic core of a tumor. Through the use of a highly sensitive and specific non-destructive US imaging paradigm, this nonlinear signal enables real-time monitoring of the precise locations of these cells in the tumor and is sufficiently stable to image tissue biodistribution and gene expression functionality over multiple days. These results represent a major improvement over previous work with heterologous GV expression in bacteria, which required the bacteria to be cultured and pre-express GVs under ideal laboratory conditions before *in vivo* injection for transient imaging.[6]

With these major improvements, we anticipate that ARGs will be useful for many applications that demand the long-term, noninvasive imaging of bacteria deep inside the body. Potential applications involve tracking therapeutic bacteria as they home to and attack tumors or travel through the gastrointestinal (GI) tract and report on its inflammatory state.[31,32] Further, the nonlinear signal generation of these ARGs mean that they could form the basis for acoustic biosensors of more dynamic cellular signals such as enzyme activity.[33]

While these results represent an important step in the development of ARGs, additional improvements could further expand their utility in biotechnology. First, the expression kinetics of ARGs are significantly slower than those of fluorescent proteins in *E. coli*,[34] and faster expression would facilitate the imaging of more dynamic genetic outputs. Second, the ability to multiplex different "colors" of ARGs nondestructively *in vivo* would enable discrimination of different strains of engineered bacteria in a consortium.[35-37] Additionally, the *Serratia* gene cluster is relatively large, making it more challenging to clone and incorporate with other genetic elements. The engineering of a shorter cluster with similar acoustic properties would simplify these efforts.

Our phylogenetic screening approach was successful in identifying bARG$_{Ser}$ as a vastly improved ARG construct for expression in *E. coli*. However, out of practical necessity, this screen only subsampled the available phylogenetic space. Future mining of additional GV-encoding gene clusters could thus lead to the discovery of ARGs with further new and improved properties. Improvements can also be made in the screening strategy. It is challenging to identify all of the *gvp* genes in a given genome (see methods), and there is considerable regulation of GV cluster transcription by factors inside[5,16] or outside[17] the clusters. In a given cloned cluster, it is possible that either essential genes are missing or cryptic regulatory elements

are included.[5,14,18] These issues could be resolved by synthesizing multiple versions of each putative gene cluster and screening a larger number of them in higher throughput. Even with optimal genetic constructs, it is likely that gene clusters from some species will not successfully form GVs in a given heterologous host due to differences in growth temperature, turgor pressure or the presence or absence of specific host factors. The phylogenetic screening strategy used in this study could thus be adapted to find optimal ARGs for use in other bacterial species of interest to the mammalian microbiome and probiotic research communities.

Just as improvements in and adaptations of fluorescent proteins enabled a wide range of microscopy applications that were mere speculations when GFP was first harnessed as a biotechnology, the systematic development of next-generation ARGs will help bring to reality the promise of sensitive, high-resolution noninvasive imaging of cellular function inside intact mammals.

MATERIALS AND METHODS

Genomic mining of ARG clusters

A literature search was conducted to find papers reporting the production of gas vesicles in any species. Search terms included "gas vesicle," "gas vacuole," "aerotope," and "aerotype." All species found are listed in **Table S1**. If the report did not include a strain name, then any available 16S rRNA gene sequence used (as it was assumed that any other strain of the same species would fall in the same place on the phylogenetic tree), but no GV gene cluster sequence was used (even if it was available for one or more strains of that species) because it was found during our analysis that: 1) several reports describe species for which some strains produce GVs but others don't, and 2) comparison of GV gene cluster sequences of multiple strains of the same species almost always showed differences—often very significant ones. Further, even if a reference stating that a given organism produced GVs was not available, 16S rRNA gene sequences from all members of the following genera were included because GV production is a diacritical taxonomic feature for these genera: *Dolichospermum*,[38] *Limnoraphis*[39] and *Planktothrix*.[40]

GV clusters were identified in genomes through a combination of annotations and sequence similarity to known *gvp* genes. However, there were two challenges in identifying all *gvp*s in a given genome: 1) there is little to no annotation for many *gvp*s, and 2) GV gene clusters are not always contiguous in genomes, and *gvp*s can occasionally be found hundreds of kb away from the main cluster(s). We attempted to only select "well-behaved" GV clusters for testing (*i.e.*, ones in which all *gvp*s identified in that genome were present in clusters, and these clusters contained a minimum of non-*gvp* genes, which could increase the metabolic burden of cluster expression without increasing GV yield), but it is possible that even for these clusters, some *gvp*s were not cloned.

Of our list of 288 strains reported to form gas vesicles, 270 had 16S rRNA gene sequences available (**Table S1**). These were downloaded from NCBI using a custom Python script, and a multiple sequence alignment was constructed using Clustal Omega.[41] This alignment was used to generate a phylogenetic tree file using ClustalW2,[42] which was rendered using EvolView.[43] Only unique species are displayed in the phylogenetic trees in **Fig. 1a** and **Fig. S1**.

Plasmid construction and molecular biology

Organisms were obtained from commercial distributors as indicated in **Table S2**. If an organism was shipped as a liquid culture, the culture was centrifuged and the pellet resuspended in ddH2O, as it was found that even trace amounts of certain culture media could completely inhibit PCR. Fragments were amplified by PCR using Q5 polymerase and assembled into a pET28a(+) vector (Novagen) via Gibson Assembly using reagents from New England Biolabs (NEB). Sub-cloning and other modifications to plasmids were also performed with Gibson Assembly using reagents from NEB. Assemblies were transformed into NEB Stable *E. coli*. All constructs were verified by Sanger sequencing.

Halobacterium salinarum has two chromosomal GV gene clusters (plus additional plasmid-borne ones), which were cloned and tested separately. *Methanosarcina vacuolata* has only one cluster, but while its genome sequence in the NCBI database has two copies of *GvpA1* and one copy of *GvpA2*, our genomic PCR yielded a product with only one copy of *GvpA1*. In a second cloning step, we added a copy of *GvpA2* to the cloned cluster. While we were able to PCR *GvpA2* from the genome, it was not contiguous with the rest of the cluster. Therefore, we speculate that either there was an error in the assembly of the genome sequence (likely caused by the high sequence similarity of the *GvpA* genes), or that the genotype of our strain differs slightly from that of the strain sequenced.

In vitro bacterial expression of ARGs

For initial testing, all constructs were expressed in BL21(DE3) *E. coli* (NEB). Fifty µL of electrocompetent *E. coli* were transformed with 1.5 µL of purified plasmid DNA (Econospin 96-well filter plate, Epoch Life Science), and 1 mL of SOC medium (NEB) was added immediately after electroporation. These cultures were incubated at 37°C for 2 hr, and 150 uL was inoculated into larger 1.5 mL LB cultures containing 100 ug/mL kanamycin and 1% (w/v) glucose in a deep-well 96-well plate and grown overnight in a shaking incubator at 30°C. Square dual-layer LB agar plates were prepared as described previously,[6] with varying concentrations of IPTG and 100 ug/mL kanamycin in the bottom layer, and 1% (w/v) glucose and 100 ug/mL kanamycin in the top layer. LB agar was incubated at 60°C for 12-36 hr after dissolution to allow it to degas. After the agar solidified, plates were dried at 37°C to remove all condensation on the top layer that would cause the bacterial patches to run together. A multichannel pipette was used to thoroughly mix overnight cultures and drop 1 µL of each culture onto the surface of the dual-layer plates, with care taken to avoid puncturing the agar which results in artifacts during ultrasound scans. Importantly, low-retention pipette tips were used, as it was found that the small volumes of culture would wet the outsides of standard pipette tips, resulting in inaccurate volume

dispensing. Patches were allowed to dry completely before plates were flipped and incubated at 37°C for 24 hr or 30°C for 48 hr.

For *in vitro* expression experiments in EcN, the appropriate plasmids were first transformed via electroporation and the outgrowth was plated on LB (Miller)-agar plates with the appropriate antibiotic (25 μg/mL chloramphenicol or 50 μg/mL kanamycin) and 1% (w/v) glucose. The resulting colonies were used to inoculate 2 mL LB (Miller) medium with the appropriate antibiotic and 1% (w/v) glucose, and these cultures were incubated at 250 rpm and 37°C overnight. Glycerol stocks were prepared by mixing the overnight cultures in a 1:1 volume ratio with 50% (v/v) glycerol and storing at -80°C. The night before expression experiments, glycerol stocks were used to inoculate overnight cultures (2 mL LB medium with the appropriate antibiotic and 1% (w/v) glucose) which were incubated at 37°C and shaken at 250 rpm. For expression on solid media, 1 μL of overnight culture was dropped onto square dual-layer LB agar plates with 2X the final inducer (IPTG, aTc, or L-arabinose) concentration in the bottom layer, 1% (w/v) glucose in the top layer, and the appropriate antibiotic in both layers (50 μg/mL chloramphenicol or 100 μg/mL kanamycin). Plates were allowed to dry, and then inverted and incubated at 37°C for 24 hours before imaging with ultrasound. For expression in liquid media, 500 μL of each overnight culture was used to inoculate 50 mL LB supplemented with 0.4% (w/v) glucose and 25 μg/mL chloramphenicol in 250 mL baffled flasks. Cultures were incubated at 37°C and 250 rpm until reaching at OD_{600} of 0.1 - 0.3. At this point, cultures were induced by addition of L-arabinose and placed back at 37°C and 250 rpm. For time titration experiments, 0.1% (w/v) L-arabinose was used for induction and 0.5 mL of each culture was removed at 0, 1, 3, 5, 7, 9, 11, and 24 hours post-induction for OD_{600} and ultrasound measurements. For L-arabinose titration experiments, L-arabinose concentrations ranging from 0 to 1% (w/v) were used for induction, and cultures were incubated for 24 hours at 37°C and 250 rpm after addition of L-arabinose before ultrasound imaging. For cell concentration titration experiments, cultures were incubated for 24 hours at 37°C and 250 rpm after addition of 0.1% (w/v) L-arabinose before ultrasound imaging. All cultures were stored at 4°C or on ice until casting in phantoms and imaging with ultrasound. In all liquid culture experiments, cultures were prescreened for the presence of GVs by phase contrast microscopy before being imaged with ultrasound.

To assess plasmid stability of pBAD-$bARG_{Ser}$-axetxe in EcN, the glycerol stock of this strain was used to inoculate 2 mL LB (Miller) supplemented with 25 μg/mL chloramphenicol and 1% (w/v) glucose, and this culture was incubated at 37°C and 250 rpm overnight. Twenty μL of the overnight culture was subcultured into 2 mL LB with 25 μg/mL chloramphenicol, 2 mL LB without antibiotics, and 2 mL LB without antibiotics and with 0.1% (w/v) L-arabinose, each in quadruplicate. Every 24 hours, 20 μL of each culture was sub-cultured into fresh media of the same conditions. All cultures were incubated at 37°C and 250 rpm. On days 1-3, 5, and 7, serial dilutions of each culture were plated on LB-agar without antibiotics, LB-agar with 25 μg/mL chloramphenicol, and LB-agar with 25 μg/mL chloramphenicol + 0.1% (w/v) L-arabinose + 0.4% (w/v) glucose. Plates were incubated at 37°C for at least 16 hours and colonies were counted and screened manually. Plasmid retention was assessed by taking the ratio of CFUs on LB-agar plates with chloramphenicol to CFUs on LB-agar plates without antibiotics. The presence of mutations that disrupt the ability to express functional $bARG_{Ser}$ was assessed by a loss of colony opacity on LB-agar plates with 25 μg/mL chloramphenicol + 0.1% (w/v) L-arabinose + 0.4% (w/v) glucose.

In vitro ultrasound imaging of bacteria expressing ARGs on solid media

Ultrasound imaging of bacterial patches was performed using a Verasonics Vantage programmable ultrasound scanning system and an L10-4v 128-element linear array transducer (Verasonics) with a center frequency of 6 MHz and an element pitch of 300 μm. Image acquisition was performed using a custom imaging script with a 64-ray-lines protocol and a synthetic aperture of 65 elements. The transmit waveform was set to a voltage of 50 V and a frequency of 10 MHz, with 1 waveform cycle and 67% intra-pulse duty cycle. In xAM mode, a custom sequence detailed previously[13] was used with an angle of 19.5°. RF data from 4 repeated acquisitions was coherently averaged prior to beamforming for each image plane.

Agar plates containing bacterial patches were coated with a thin layer of LB agar and immersed in PBS to allow acoustic coupling to the L10-4v transducer. The transducer was connected to a BiSlide computer-controlled 3D translatable stage (Velmex) and positioned above the plane of the plate at an angle of 15° from the vertical (to minimize specular reflection from the plastic dishes and agar) and a distance of 20 mm from the bacterial patches. The imaging sequence was applied sequentially to acquire image planes covering the full area of all plates. A custom script was used to automate the scan by controlling the motor stage in tandem with the ultrasound system, translating 0.5 mm in the azimuthal direction between rows and 19.5 mm in the lateral direction between columns. In the case of pre-minus-post-collapse scans, the full scan sequence was repeated after returning the motor stage to its origin and adjusting the voltage of the transducer.

For image processing and analysis, custom beamforming scripts were applied on-line to reconstruct image planes from the acquired RF data at each location. The intensity data for each plane was saved for off-line processing. All image planes were concatenated to form a 3D volume with all plates and colonies. A 2D image of the colonies was extracted from the 3D volume by taking the maximum intensity over a manually-defined depth range for all voxel columns. 2D pre-minus-post-collapse images were obtained by subtracting the post-collapse 2D image from the pre-collapse 2D image. Bacterial patch intensities were then quantified from these 2D images. Sample ROIs were drawn around the center of each patch to avoid artefacts from the edges, and background ROIs were drawn around representative regions without patches. The signal-to-background ratio (SBR) was calculated as the mean pixel intensity of the sample ROI divided by the mean pixel

intensity of the background. Conversion to decibels (dB) was calculated as 20*log10(SBR). For display, images were normalized by dividing by the average background signal of all images being compared and setting the lower and upper limits of the colormaps to be the same, where the lower limit was equal to a constant A times the average background and the upper limit was equal to a constant B times the maximum pixel intensity out of all images being compared; images were then converted to dB. For xAM and pre-minus-post-collapse xAM images of bacterial patches, A was set to 1 and B was set to 0.5.

In vitro ultrasound imaging of bacteria expressing ARGs suspended in agarose phantoms

To create phantoms for ultrasound imaging of bacteria from liquid cultures or suspended in PBS from patches on solid media, wells were cast with a custom 3D-printed mold using 1% (w/v) agarose in PBS, which was degassed by incubating at 60°C for at least 16 hours. Cultures or cell suspensions to be analyzed were diluted in ice-cold PBS to 2x the final desired cell concentration (calculated from the measured OD_{600}), incubated at 42°C for one minute, and mixed 1:1 with 1% (w/v) agarose in PBS at 42°C for a final concentration of 1x. This mixture was then loaded into the wells in duplicate and allowed to solidify. Care was taken not to introduce bubbles during this process. The phantoms were submerged in PBS, and ultrasound images were acquired using a Verasonics Vantage programmable ultrasound scanning system and an L22-14v 128-element linear array transducer with a center frequency of 18.5 MHz with 67%-6-dB bandwidth, an element pitch of 100 µm, an elevation focus of 8 mm, and an elevation aperture of 1.5 mm. The transducer was attached to a custom-made manual translation stage to move between samples. B-mode and xAM images were acquired using the same parameters as described previously[33]: the frequency and transmit focus were set to 15.625 MHz and 5 mm, respectively, and each image was an average of 50 accumulations. B-mode imaging was performed with a conventional 128-ray-lines protocol, where each ray line was a single pulse transmitted with an aperture of 40 elements. xAM imaging was performed using a custom sequence detailed previously[13] with an angle of 19.5° and an aperture of 65 elements. The transmitted pressure at the focus was calibrated using a Fibre-Optic Hydrophone (Precision Acoustics), and the peak positive pressure was used as the "acoustic pressure" in Fig. 3.

To measure the xAM signal at varying acoustic pressures, an automated voltage ramp imaging script was used to acquire an xAM image at each voltage step (0.5 V increments from 2 to 25 V), immediately followed by a B-mode acquisition at a constant voltage of 1.6 V (0.15 MPa) before another xAM acquisition at the next voltage step; the voltage was held constant for 10 seconds at each step before the image was saved. To measure the xAM and B-mode signals over time at various acoustic pressures, another script was used to automatically save an xAM or B-mode image every second while the voltage was automatically increased by 2 V approximately every 70 seconds. Each frame consisted of 64 ray lines, which took 180 µs each to acquire, giving a pulse repetition rate of 86.8 Hz. Based on these results, all subsequent *in vitro* xAM images of $bARG_{Ser}$-expressing EcN were acquired at 18V (1.29 MPa).

Image processing and analysis were performed as described above, except that custom beamforming scripts were applied off-line to reconstruct images from the saved RF data for each sample, no 3D reconstruction was performed as images captured at single locations, circular ROIs were drawn around sample and background regions (taking care to avoid bubbles) to calculate SBRs, and values of A=1.4 and B=0.5 were used to normalize images for display.

Microscopy

For TEM imaging, cells expressing GVs were diluted to OD_{600} ~1 in 10 mM HEPES (pH 7.5) or culture media. 3 µL of the sample was applied to a freshly glow-discharged (Pelco EasiGlow, 15 mA, 1 min) Formvar/carbon-coated, 200 mesh copper grid (Ted Pella) for 1 min before being reduced to a thin film by blotting. Grids with cells were washed three times in 10 mM HEPES (pH 7.5), blotted, air-dried, and imaged without the stain. Image acquisition was performed using a Tecnai T12 (FEI, now Thermo Fisher Scientific) electron microscope operated at 120 kV, equipped with a Gatan Ultrascan 2k X 2k CCD. For phase contrast microcopy (PCM) imaging, cells expressing GVs were scraped off from plates and re-suspended in PBS at an OD_{600} of 1-2. Suspensions were transferred to glass slides and PCM images were acquired using a Zeiss Axiocam microscope with a 40X Ph2 objective.

In vivo bacterial ARG expression and ultrasound imaging

All *in vivo* experiments were performed under a protocol approved by the Institutional Animal Care and Use of Committee (IACUC) of the California Institute of Technology. For experiments involving tumor colonization with EcN, MC26 cells were grown in DMEM media in T225 flasks. After trypsinization and resuspension in PBS + 0.1 mg/mL DNAseI, 5 x 10^6 MC26 cells were injected subcutaneously into the right flank of 6-8 week-old female Balb/cJ mice. Tumors were allowed to grow for 14 days (reaching sizes of 200-300 mm^3) before injecting 10^8 EcN cells suspended in PBS via the lateral tail vein. The day before injection of EcN, Ibuprofen was added to the drinking water at 0.2 mg/mL to ameliorate side effects of EcN injections. To prepare the EcN for injection, the appropriate glycerol stocks were used to inoculate 2 mL LB + 1% (w/v) glucose + 25 ug/mL chloramphenicol which was incubated at 37°C and 250 rpm overnight. The overnight culture (500 µL) was used to inoculate 50 mL LB + 0.4% (w/v) glucose + 25 µg/mL chloramphenicol in 250 mL baffled flasks, which was grown at 37°C and 250 rpm until reaching an OD_{600} of 0.3 - 0.6. This culture was pelleted, washed 4 times with PBS, resuspended in PBS at an OD_{600} of 0.625, and used for injection. Three days after injection of EcN, mice were injected intraperitoneally with 120 mg L-arabinose to induce the EcN. Starting 24 hours after induction, ultrasound images of tumors were acquired as described below. After imaging, 3.0 MPa acoustic pressure was applied throughout the tumor to collapse GVs, and mice were injected again intraperitoneally with 120 mg L-arabinose. The next day, mice were imaged again with

ultrasound for re-expression of GVs. The following day, all mice were euthanized and tumors were excised, homogenized, serially diluted, and plated on selective media (LB-agar + 25 μg/mL chloramphenicol) as well as on induction plates (LB-agar + 25 μg/mL chloramphenicol + 0.4% (w/v) glucose + 0.1% (w/v) L-arabinose). Colonies on plates with chloramphenicol were manually counted to quantify the levels of colonization, and colonies on induction plates were screened for a non-opaque mutant phenotype.

For ultrasound imaging, mice were anesthetized with 2% isoflurane and maintained at 37°C using a heating pad. Images were acquired using the L22-14v transducer attached to a manual translation stage described above. Any hair on or around the tumors was removed with Nair, and Aquasonic 100 ultrasound transmission gel was used to couple the transducer to the skin. B-mode and parabolic AM (pAM) images were first acquired using a custom 128 ray line script. Each image was formed from 96 focused beam ray lines, each with a 32-element aperture and 6 mm focus. The transmit waveform was set to a voltage of 1.6V in B-mode or 8V in pAM and a frequency of 15.625 MHz, with 1 waveform cycle and 67% intra-pulse duty. In B-mode, each ray line was a single transmit with all 32 elements, and in pAM each ray line consisted of one transmit with all 32 elements followed by 2 transmits in which first the odd and then the even-numbered elements are silenced.[44] Subsequently, xAM images and additional B-mode images were acquired at the same location without moving the transducer using the same parameters as described above for the *in vitro* experiments (e.g. 18V for xAM and 1.6V for B-mode). At least two separate locations spaced at least 2 mm apart in each tumor were imaged with B-mode, pAM, and xAM. Ultrasound images of tumors were quantified as described above where the sample ROIs were drawn around the necrotic cores in the tumors and the background ROIs were drawn around regions in the gel above the mouse. Images were normalized and plotted on a dB scale as described above except the scaling factors were A=2.5 and B=1 for pAM and the corresponding B-mode tumor images, and A=3.5 and B=1 for xAM and the corresponding B-mode tumor images.

Histology

Tumors were colonized with pBAD-bARG$_{Ser}$-axetxe EcN following the same protocol as described above. The day after inducing GV expression with IP injections of L-arabinose, xAM and B-mode images of tumors were acquired as described above. Shortly after imaging, mice were euthanized by sedation with isoflurane and cervical dislocation. Tumors were resected, placed in 10% buffered formalin for 48 hours, and then washed and stored in 70% ethanol. Tumors were then cut in half along the approximate plane of imaging, placed in tissue cassettes, and sent to the Translational Pathology Core Laboratory at UCLA, which embedded samples in paraffin and performed H&E staining, immunohistochemistry, and microscopy imaging. Immunohistochemistry was performed using Opal IHC kits (Akoya Biosciences) according to the manufacturer's instructions. Tissue sections were incubated with either polyclonal rabbit anti-*E. coli* antibody (Virostat; catalogue number 1001) or non-reactive rabbit IgG isotype control antibody as a negative control. All sections were then incubated with an Opal 520 polymer anti-rabbit HRP antibody (Akoya Biosciences) and counterstained with DAPI. Sections were imaged in the appropriate fluorescence or brightfield channels using a high throughput scanning system (Leica Aperio VERSA) with 40 μm resolution.

Data and code availability

Plasmids will be made available through Addgene upon publication. All other materials and data are available from the corresponding author upon reasonable request.

ACKNOWLEDGEMENTS

The authors would like to thank Dianne Newman for a sample of *Streptomyces coelicolor* A3(2), and Yunfeng Li and Avinoam Bar-Zion for help with tissue histology. Electron microscopy was performed in the Beckman Institute Resource Center for Transmission Electron Microscopy at Caltech. R.C.H. was supported by the Caltech Center for Environmental Microbial Interactions. M.T.B. was supported by an NSF GRFP fellowship. This research was supported by the National Institutes of Health (R01-EB018975 to M.G.S.) and Pew Charitable Trust. Related research in the Shapiro Laboratory is supported by the David and Lucille Packard Foundation, the Burroughs Wellcome Fund and the Heritage Medical Research Institute.

AUTHOR CONTRIBUTIONS

R.C.H., M.T.B., K.W., M.B.S., P.D., Z.J., and R.D. planned and performed experiments. M.T.B. performed all *in vivo* experiments, with help from M.B.S. P.D. performed TEM imaging. D.R.M. built the ultrasound plate-scanning setup, and D.R.M. and D.P.S. wrote the associated MATLAB scripts for controlling it. Z.J. and D.P.S. wrote the MATLAB scripts for ultrasound imaging of EcN *in vitro* and *in vivo*. Z.J. performed the calibration of the L22-14v transducer. M.H.A. provided the axe-txe stability cassette, and advised on tumor colonization experiments. R.C.H., M.T.B., D.P.S., P.D., and Z.J. analyzed data. R.C.H., M.T.B., and M.G.S. wrote the manuscript with input from all other authors. M.G.S. supervised the research.

COMPETING INTERESTS

The authors declare no competing financial interests.

REFERENCES

1. Piraner, D. I. *et al.* Going Deeper: Biomolecular Tools for Acoustic and Magnetic Imaging and Control of Cellular Function. *Biochemistry* **56**, 5202–5209 (2017).
2. Maresca, D. *et al.* Biomolecular Ultrasound and Sonogenetics. *Annual Review of Chemical and Biomolecular Engineering* **9**, 229–252 (2018).
3. Shapiro, M. G. *et al.* Biogenic Gas Nanostructures as Ultrasonic Molecular Reporters. *Nat Nanotechnol* **9**, 311–316 (2014).
4. Walsby, A. E. Gas vesicles. *Microbiological Reviews* **58**, 94–144 (1994).
5. Pfeifer, F. Distribution, formation and regulation of gas vesicles. *Nature Reviews Microbiology* **10**, 705–715 (2012).
6. Bourdeau, R. W. *et al.* Acoustic reporter genes for noninvasive imaging of microbes in mammalian hosts. *Nature* **553**, 86–90 (2018).
7. Farhadi, A., Ho, G. H., Sawyer, D. P., Bourdeau, R. W. & Shapiro, M. G. Ultrasound imaging of gene expression in mammalian cells. *Science* **365**, 1469–1475 (2019).
8. Chow, B. Y. *et al.* High-performance genetically targetable optical neural silencing by light-driven proton pumps. *Nature* **463**, 98–102 (2010).
9. Matz, M. V. *et al.* Fluorescent proteins from nonbioluminescent Anthozoa species. *Nature Biotechnology* **17**, 969–973 (1999).
10. Stanton, B. C. *et al.* Genomic mining of prokaryotic repressors for orthogonal logic gates. *Nature Chemical Biology* **10**, 99–105 (2014).
11. Mak, W. S. *et al.* Integrative genomic mining for enzyme function to enable engineering of a non-natural biosynthetic pathway. *Nature Communications* **6**, 10005 (2015).
12. Burstein, D. *et al.* New CRISPR–Cas systems from uncultivated microbes. *Nature* **542**, 237–241 (2017).
13. Maresca, D., Sawyer, D. P., Renaud, G., Lee-Gosselin, A. & Shapiro, M. G. Nonlinear X-Wave Ultrasound Imaging of Acoustic Biomolecules. *Phys. Rev. X* **8**, 041002 (2018).
14. Tashiro, Y., Monson, R. E., Ramsay, J. P. & Salmond, G. P. C. Molecular genetic and physical analysis of gas vesicles in buoyant enterobacteria. *Environ Microbiol* **18**, 1264–1276 (2016).
15. Oren, A., Pri-El, N., Shapiro, O. & Siboni, N. Gas vesicles isolated from Halobacterium cells by lysis in hypotonic solution are structurally weakened. *FEMS Microbiology Letters* **252**, 337–341 (2005).
16. Ramsay, J. P., Williamson, N. R., Spring, D. R. & Salmond, G. P. C. A quorum-sensing molecule acts as a morphogen controlling gas vesicle organelle biogenesis and adaptive flotation in an enterobacterium. *PNAS* **108**, 14932–14937 (2011).
17. Lee, C. M., Monson, R. E., Adams, R. M. & Salmond, G. P. C. The LacI–Family Transcription Factor, RbsR, Is a Pleiotropic Regulator of Motility, Virulence, Siderophore and Antibiotic Production, Gas Vesicle Morphogenesis and Flotation in Serratia. *Front. Microbiol.* **8**, (2017).
18. Li, N. & Cannon, M. C. Gas Vesicle Genes Identified in Bacillus megaterium and Functional Expression in Escherichia coli. *J Bacteriol* **180**, 2450–2458 (1998).
19. Li, Z. & Rinas, U. Recombinant protein production associated growth inhibition results mainly from transcription and not from translation. *Microb Cell Fact* **19**, (2020).
20. Borkowski, O., Ceroni, F., Stan, G.-B. & Ellis, T. Overloaded and stressed: whole-cell considerations for bacterial synthetic biology. *Current Opinion in Microbiology* **33**, 123–130 (2016).
21. Sleight, S. C. & Sauro, H. M. Visualization of Evolutionary Stability Dynamics and Competitive Fitness of Escherichia coli Engineered with Randomized Multigene Circuits. *ACS Synth. Biol.* **2**, 519–528 (2013).
22. Schultz, M. Clinical use of E. coli Nissle 1917 in inflammatory bowel disease. *Inflammatory Bowel Diseases* **14**, 1012–1018 (2008).
23. Stritzker, J. *et al.* Tumor-specific colonization, tissue distribution, and gene induction by probiotic Escherichia coli Nissle 1917 in live mice. *International Journal of Medical Microbiology* **297**, 151–162 (2007).

24. Sonnenborn, U. & Schulze, J. The non-pathogenic Escherichia coli strain Nissle 1917–features of a versatile probiotic. *Microbial Ecology in Health and Disease* **21**, 122–158 (2009).
25. Gurbatri, C. R. *et al.* Engineered Probiotics for Local Tumor Delivery of Checkpoint Blockade Nanobodies. *Sci Transl Med* **12**, (2020).
26. Duong, M. T.-Q., Qin, Y., You, S.-H. & Min, J.-J. Bacteria-cancer interactions: bacteria-based cancer therapy. *Experimental & Molecular Medicine* **51**, 1–15 (2019).
27. Leventhal, D. S. *et al.* Immunotherapy with engineered bacteria by targeting the STING pathway for anti-tumor immunity. *Nature Communications* **11**, 2739 (2020).
28. Zhang, Y. *et al.* E. coli Nissle 1917-Derived Minicells for Targeted Delivery of Chemotherapeutic Drug to Hypoxic Regions for Cancer Therapy. *Theranostics* **8**, 1690–1705 (2018).
29. Grady, R. & Hayes, F. Axe–Txe, a broad-spectrum proteic toxin–antitoxin system specified by a multidrug-resistant, clinical isolate of Enterococcus faecium. *Molecular Microbiology* **47**, 1419–1432 (2003).
30. Ceroni, F. *et al.* Burden-driven feedback control of gene expression. *Nature methods* **15**, 387 (2018).
31. Charbonneau, M. R., Isabella, V. M., Li, N. & Kurtz, C. B. Developing a new class of engineered live bacterial therapeutics to treat human diseases. *Nature Communications* **11**, 1738 (2020).
32. Jimenez, M., Langer, R. & Traverso, G. Microbial therapeutics: New opportunities for drug delivery. *J Exp Med* **216**, 1005–1009 (2019).
33. Lakshmanan, A. *et al.* Acoustic Biosensors for Ultrasound Imaging of Enzyme Activity. *Nat Chem Biol* **16**, 988–996 (2020).
34. Hui, C.-Y., Guo, Y., Zhang, W. & Huang, X.-Q. Rapid monitoring of the target protein expression with a fluorescent signal based on a dicistronic construct in Escherichia coli. *AMB Express* **8**, 81 (2018).
35. Alnahhas, R. N. *et al.* Majority sensing in synthetic microbial consortia. *Nature Communications* **11**, 3659 (2020).
36. Hays, S. G., Patrick, W. G., Ziesack, M., Oxman, N. & Silver, P. A. Better together: engineering and application of microbial symbioses. *Current Opinion in Biotechnology* **36**, 40–49 (2015).
37. Ziesack, M. *et al.* Engineered Interspecies Amino Acid Cross-Feeding Increases Population Evenness in a Synthetic Bacterial Consortium. *mSystems* **4**, (2019).
38. Wacklin, P., Hoffmann, L. & Komárek, J. Nomenclatural validation of the genetically revised cyanobacterial genus Dolichospermum (RALFS ex BORNET et FLAHAULT) comb. nova. *Fottea* **9**, 59–64 (2009).
39. Komárek, J. *et al.* Polyphasic evaluation of Limnoraphis robusta, a water-bloom forming cyanobacterium from Lake Atitlán, Guatemala, with a description of Limnoraphis gen. nov. *Fottea* **13**, 39–52 (2013).
40. Komárek, J. Planktic oscillatorialean cyanoprokaryotes (short review according to combined phenotype and molecular aspects). in *Phytoplankton and Equilibrium Concept: The Ecology of Steady-State Assemblages* (eds. Naselli-Flores, L., Padisák, J. & Dokulil, M. T.) 367–382 (Springer Netherlands, 2003). doi:10.1007/978-94-017-2666-5_30.
41. Sievers, F. *et al.* Fast, scalable generation of high-quality protein multiple sequence alignments using Clustal Omega. *Molecular Systems Biology* **7**, 539 (2011).
42. Larkin, M. A. *et al.* Clustal W and Clustal X version 2.0. *Bioinformatics* **23**, 2947–2948 (2007).
43. Subramanian, B., Gao, S., Lercher, M. J., Hu, S. & Chen, W.-H. Evolview v3: a webserver for visualization, annotation, and management of phylogenetic trees. *Nucleic Acids Research* **47**, W270–W275 (2019).
44. Maresca, D. *et al.* Nonlinear ultrasound imaging of nanoscale acoustic biomolecules. *Appl Phys Lett* **110**, (2017).

Supplementary Information

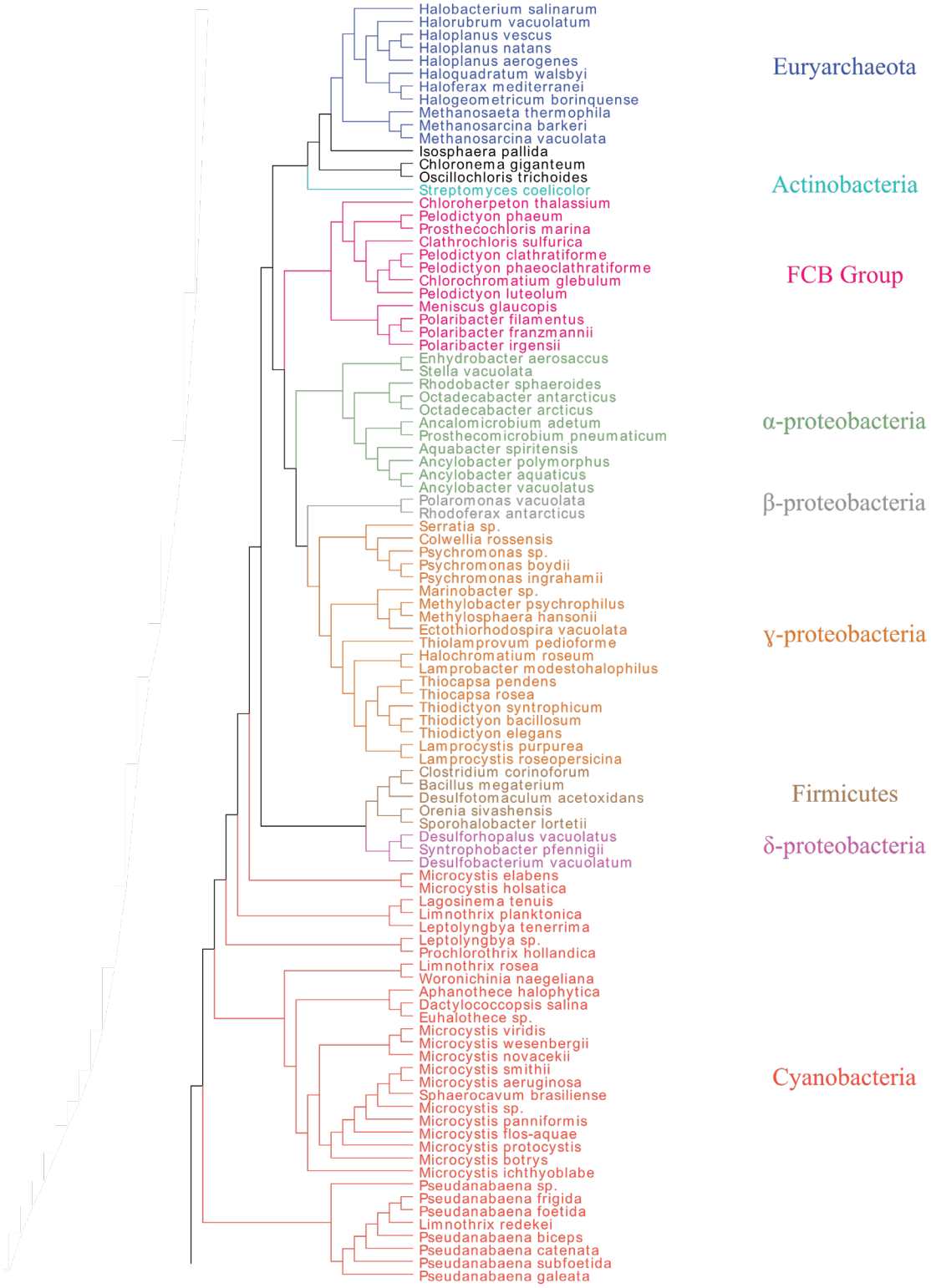

Figure S1 | 16S phylogenetic tree of all reported GV-producing organisms. Colors indicate groupings of phylogenetically similar organisms. Organisms from which GV genes were tested in *E. coli* are shown in **Fig. 1a**.

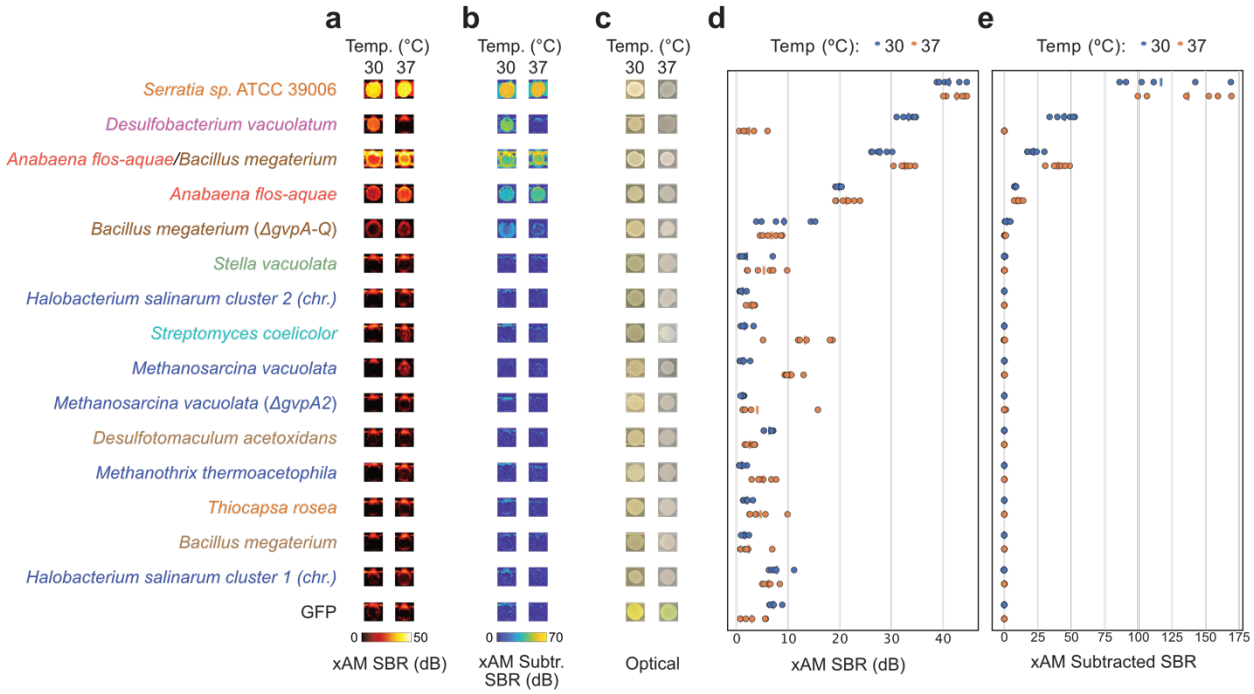

Figure S2 | Additional images and quantification of *E. coli* patches expressing select GV gene clusters. (a-c) xAM images (a), pre-minus-post-collapse xAM images (b), and optical images showing opacity (c) of patches of *E. coli* expressing various GV gene clusters from the organisms listed on the left. **(d-e)** Quantification of the xAM (d) and pre-minus-post-collapse xAM (e) signals from images in (a-b) (n=6). SBR, signal-to-background ratio.

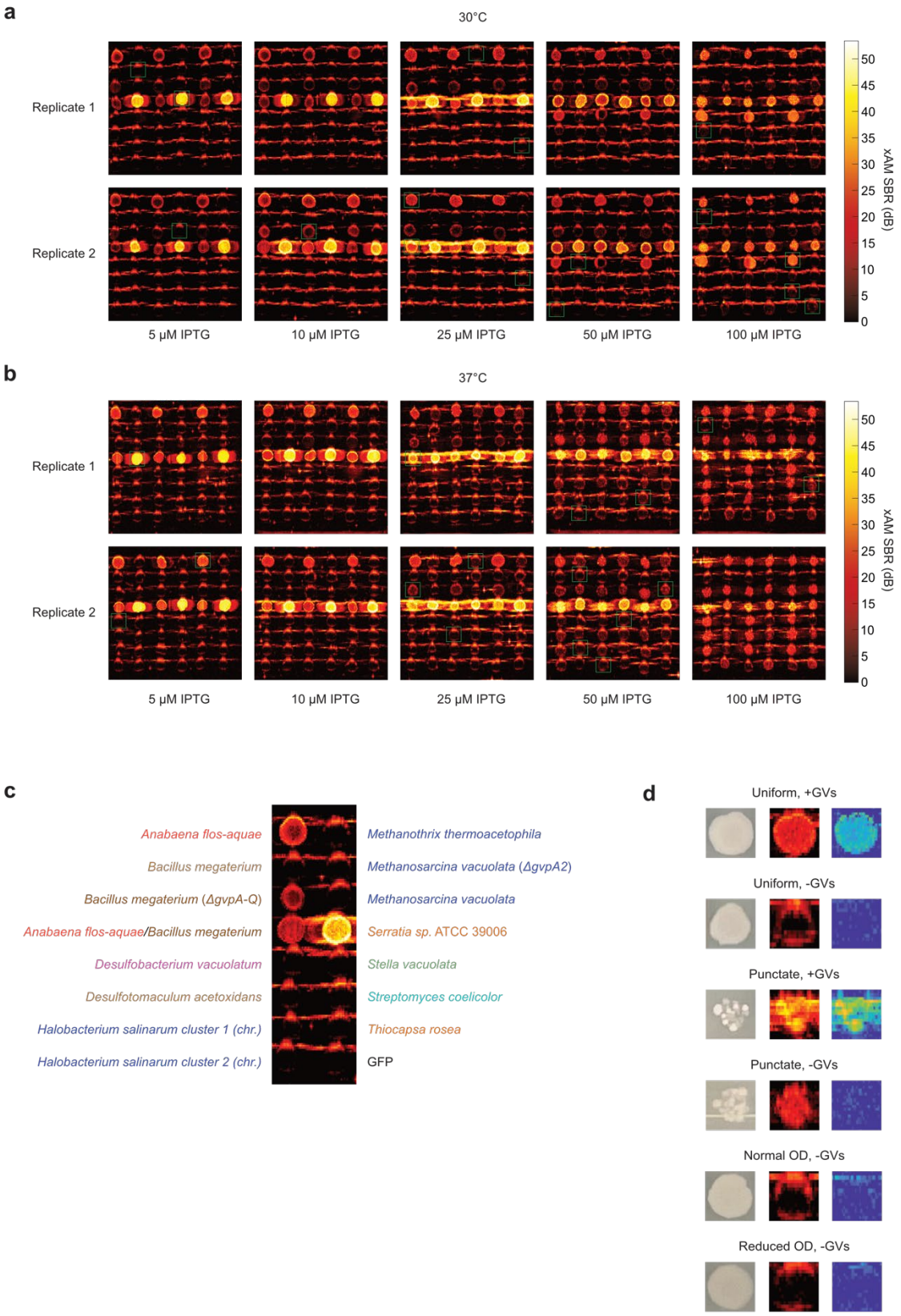
a
30°C
Replicate 1
Replicate 2
5 μM IPTG
10 μM IPTG
25 μM IPTG
50 μM IPTG
100 μM IPTG
xAM SBR (dB)
b
37°C
Replicate 1
Replicate 2
5 μM IPTG
10 μM IPTG
25 μM IPTG
50 μM IPTG
100 μM IPTG
xAM SBR (dB)
c
Anabaena flos-aquae
Bacillus megaterium
Bacillus megaterium (ΔgvpA-Q)
Anabaena flos-aquae/Bacillus megaterium
Desulfobacterium vacuolatum
Desulfotomaculum acetoxidans
Halobacterium salinarum cluster 1 (chr.)
Halobacterium salinarum cluster 2 (chr.)
Methanothrix thermoacetophila
Methanosarcina vacuolata (ΔgvpA2)
Methanosarcina vacuolata
Serratia sp. ATCC 39006
Stella vacuolata
Streptomyces coelicolor
Thiocapsa rosea
GFP
d
Uniform, +GVs
Uniform, -GVs
Punctate, +GVs
Punctate, -GVs
Normal OD, -GVs
Reduced OD, -GVs

Figure S3 | Optimization of expression conditions for all tested clusters in BL21(DE3) *E. coli*. (**a-b**) xAM images of bacterial patches expressing each GV cluster at varying inducer concentrations and temperatures. Green boxes indicate the patches shown in **Fig. S2a**. The IPTG concentration selected was the one that resulted in the highest xAM pre-minus-post-collapse difference signal (**Fig. S6**) while not creating toxicity, as determined by whether the patch was uniform or punctate (**Fig. S5a-b**). Some of the IPTG concentrations that led to toxicity also created significant xAM signal, but this signal did not originate from GVs, as indicated by the lack of xAM pre-minus-post-collapse signal difference (**Fig. S6**). Further, there were some IPTG concentrations for certain genotypes that created significant xAM signal but no xAM pre-minus-post-collapse signal difference, and no visible toxicity (e.g., *Streptomyces coelicolor*, *Thiocapsa rosea*, and GFP at 37˚C, 100 μM IPTG). This discrepancy was likely caused by subtle toxicity that is not apparent in optical images, but altered the texture of the patch enough to be detectable by US. (**c**) Key for genotypes tested in (a-b), with this pattern repeated in three pairs of columns replicated on each plate. (**d**) Examples of the effects of toxic genotypes on bacterial patches, and of artifacts that can appear in bacterial patch scan images. Bacteria themselves can produce significant xAM signal (especially when present in extremely high concentrations, as they are in the confluent patches imaged here), which can be seen in the forms of rings around all patches, regardless of GV expression status. Further, expression of toxic proteins (or of large amounts of otherwise non-toxic proteins, such as GFP) can interfere with bacterial growth; in extreme cases this results in significant cell death and a punctate appearance, and in less extreme cases it simply reduces the optical density of patches. GV expression can increase the optical density of patches, but only at high levels of GV expression. Punctate patches produce considerably more xAM signal than uniform ones, even in the absence of GV expression. The xAM pre-minus-post-collapse difference can be used to qualitatively determine if a patch produces GVs, but because collapse is incomplete in some cases, it is not an ideal method for quantitatively comparing genotypes.

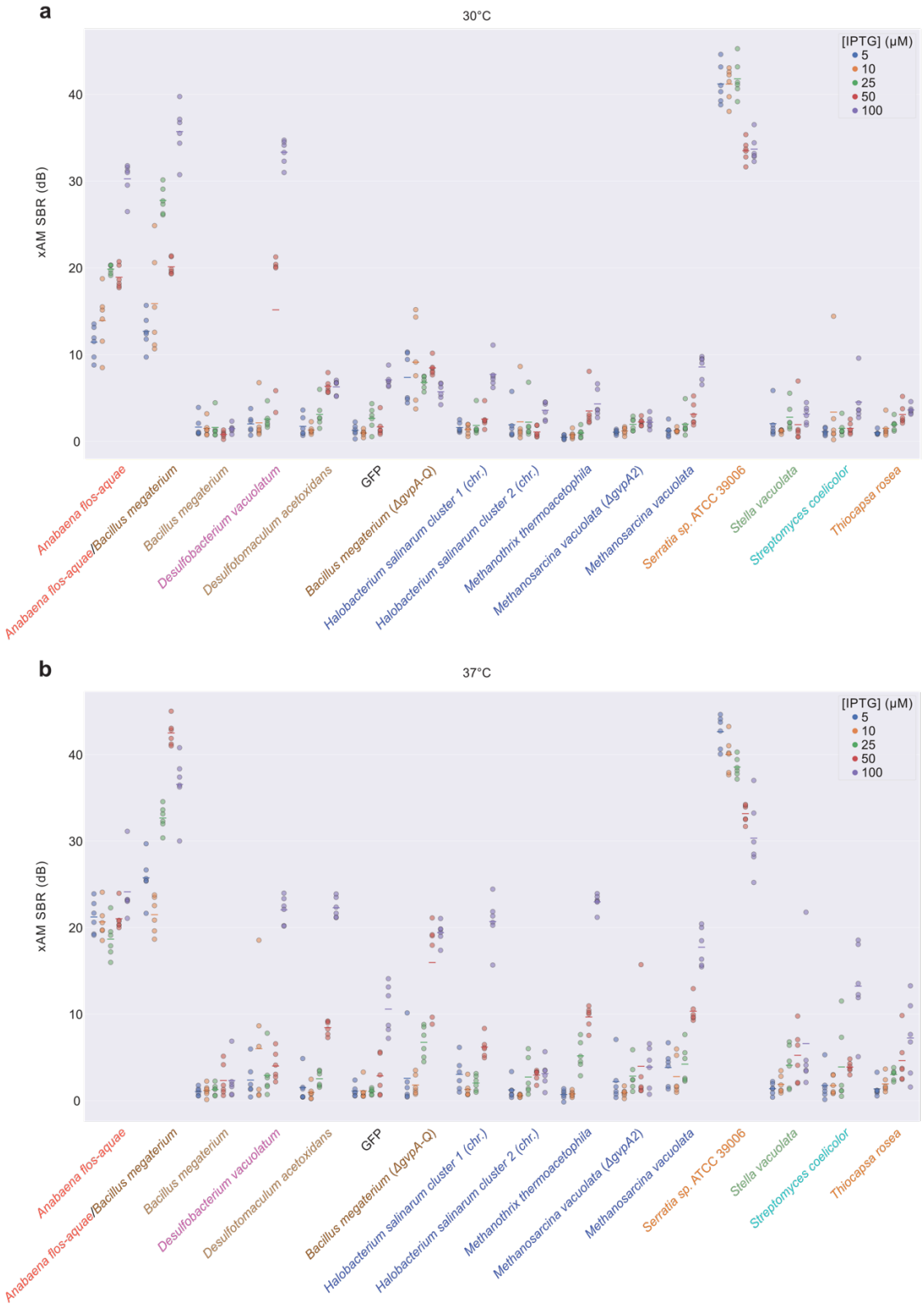

Figure S4 | Quantification of ultrasound signal for all samples shown in Fig. S3a-b. (a-b) xAM SBR of the patches at 30°C (a) and 37°C (b) shown in **Fig. S3a-b**.

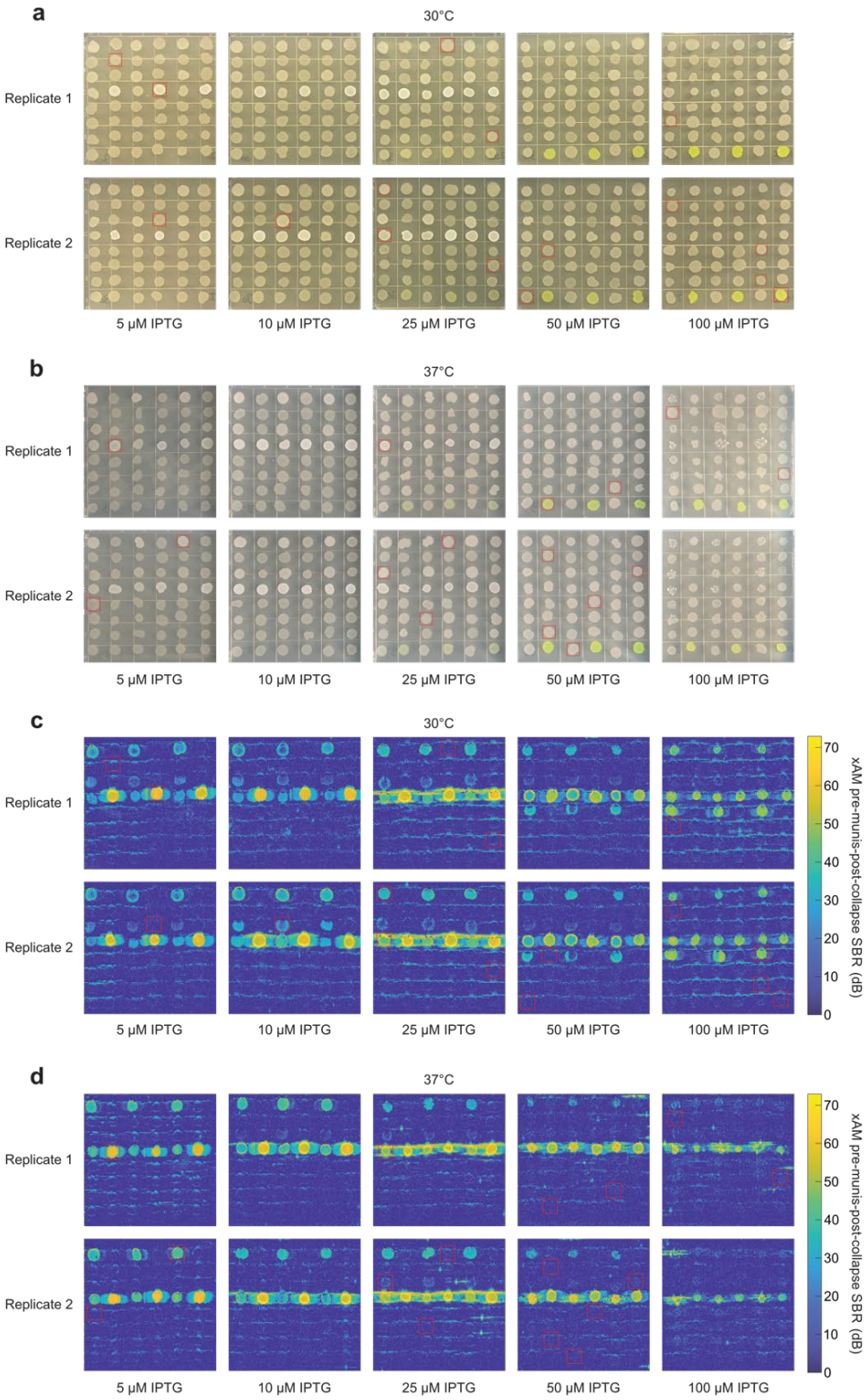

Figure S5 | Optical and xAM pre-minus-post-collapse difference images of all samples shown in Fig. S3. (**a-b**) Optical images of patches at 30°C (a) and 37°C (b) shown in **Fig. S3a-b**. (**c-d**) xAM pre-minus-post-collapse difference patches of samples at 30°C (a) and 37°C (b) shown in **Fig. S3a-b**. Red boxes indicate the patches shown in **Fig. S2b-c**.

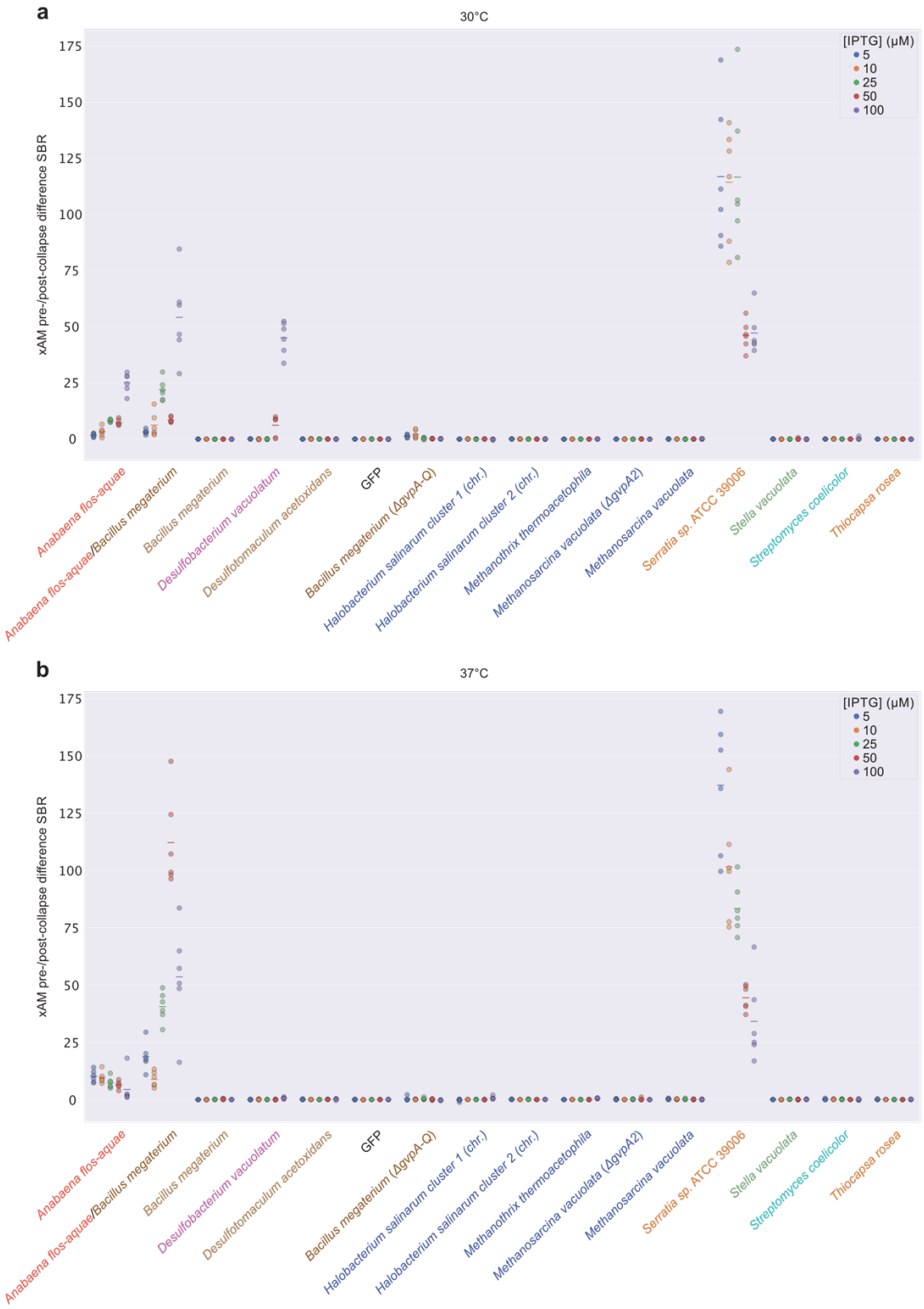

Figure S6 | Quantification of ultrasound signal for samples shown in Fig. S5c-d. (a-b) xAM SBR for the patches at 30°C (a) and 37°C (b) shown in **Fig. S5c-d.**

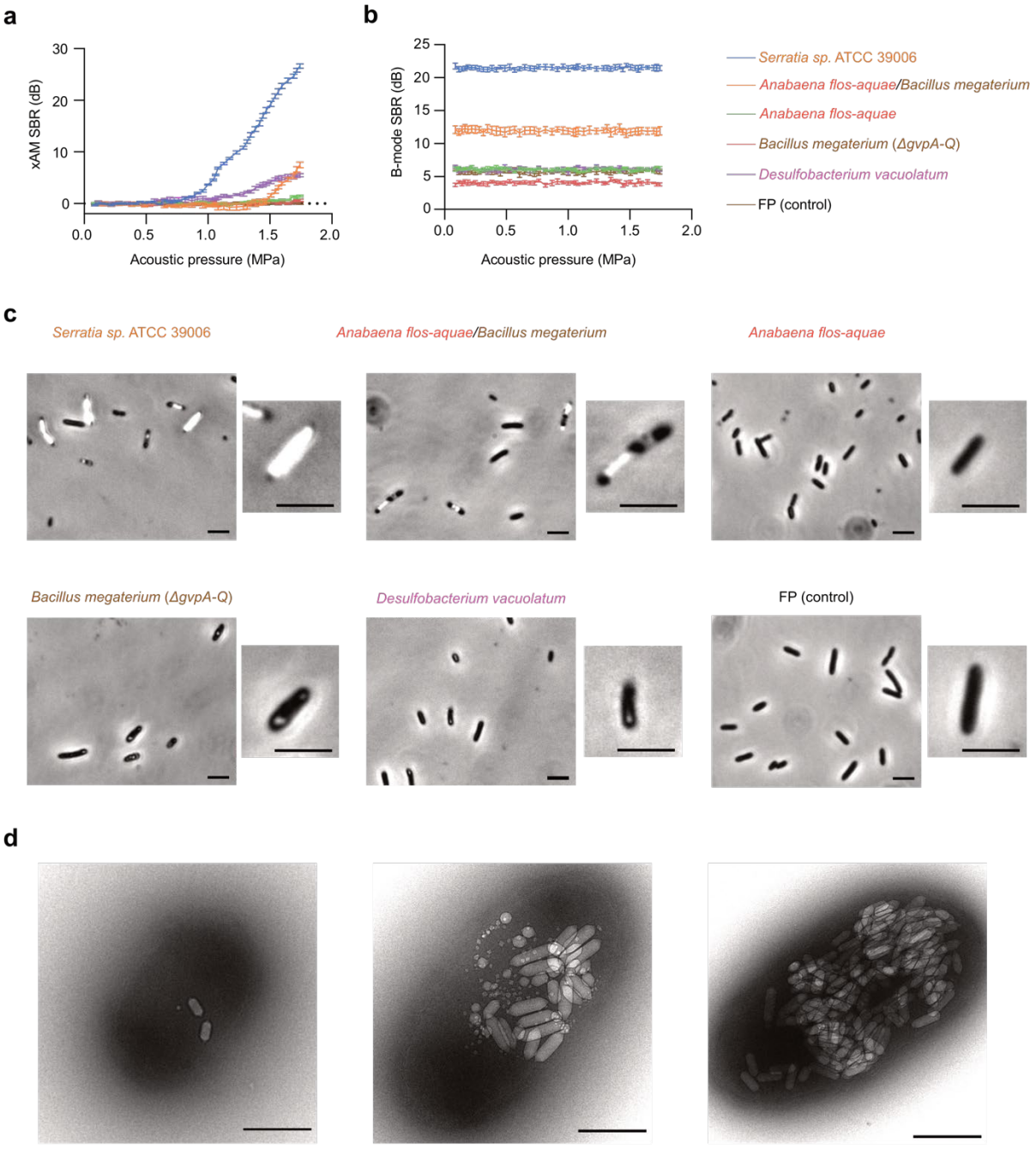

Figure S7 | Characterization of working GV clusters in BL21(DE3) *E. coli*. (a-c) xAM signal-to-background ratio (SBR) as a function of acoustic pressure (a), B-mode SBR at a constant pressure of 0.15 MPa after each increase in acoustic pressure in a (b), and representative phase contrast microscopy (PCM) images (c) of the working GV clusters expressed in BL21(DE3) *E. coli* at 30°C on solid media. For ultrasound imaging (a-b), samples were normalized to 5 x 10^9 cells/mL in agarose phantoms. Curves and error bars represent the mean (n=3 biological replicates each with 2 technical replicates) ± SEM. (a-b) have the same legend. GV clusters in cells are visible by PCM for all clusters except for the cluster from *Anabaena flos-aquae* and the fluorescent protein (FP) control (c). (d) Representative TEM images of BL21(DE3) *E. coli* cells expressing Serratia GVs at varying levels of expression. Scale bars are 5 µm in (c) and 500 nm in (d).

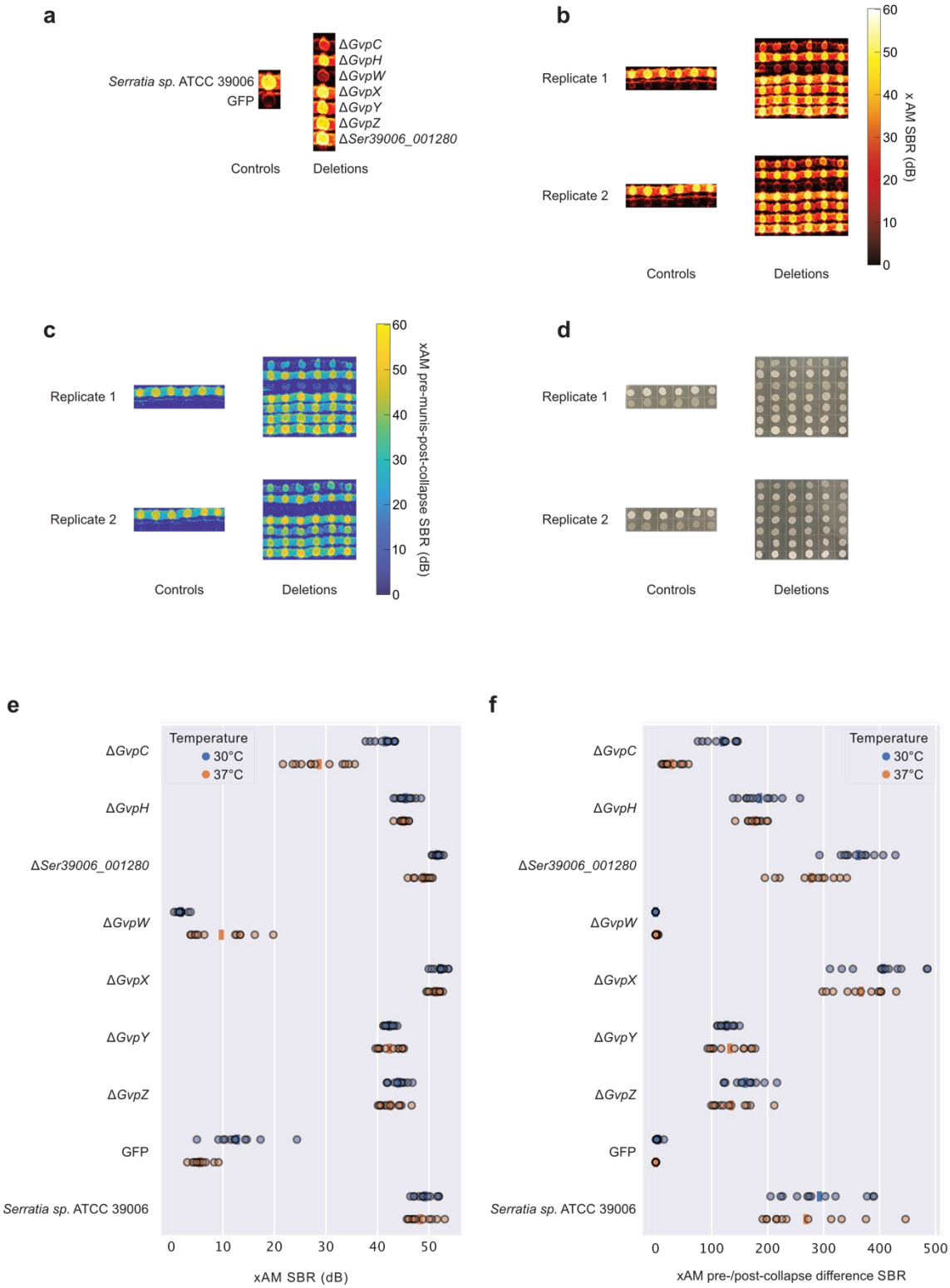
a
Serratia sp. ATCC 39006
GFP
ΔGvpC
ΔGvpH
ΔGvpW
ΔGvpX
ΔGvpY
ΔGvpZ
ΔSer39006_001280
Controls
Deletions
b
Replicate 1
Replicate 2
Controls
Deletions
x AM SBR (dB)
c
Replicate 1
Replicate 2
Controls
Deletions
xAM pre-munis-post-collapse SBR (dB)
d
Replicate 1
Replicate 2
Controls
Deletions
e
Temperature
30°C
37°C
ΔGvpC
ΔGvpH
ΔSer39006_001280
ΔGvpW
ΔGvpX
ΔGvpY
ΔGvpZ
GFP
Serratia sp. ATCC 39006
xAM SBR (dB)
f
Temperature
30°C
37°C
ΔGvpC
ΔGvpH
ΔSer39006_001280
ΔGvpW
ΔGvpX
ΔGvpY
ΔGvpZ
GFP
Serratia sp. ATCC 39006
xAM pre-/post-collapse difference SBR

Figure S8 | Effects of single-gene deletions on GV expression by the *Serratia* cluster. (**a**) Key for genotypes tested, repeated in 6 replicate columns on each plate. (**b-d**) xAM images (b), pre-minus-post-collapse xAM images (c), and optical images (d) of bacterial patches expressing single-gene deletions of the Serratia cluster. (**e-f**) Quantification of the xAM images (e) and pre-minus-post-collapse xAM images (f) shown in (b-c).

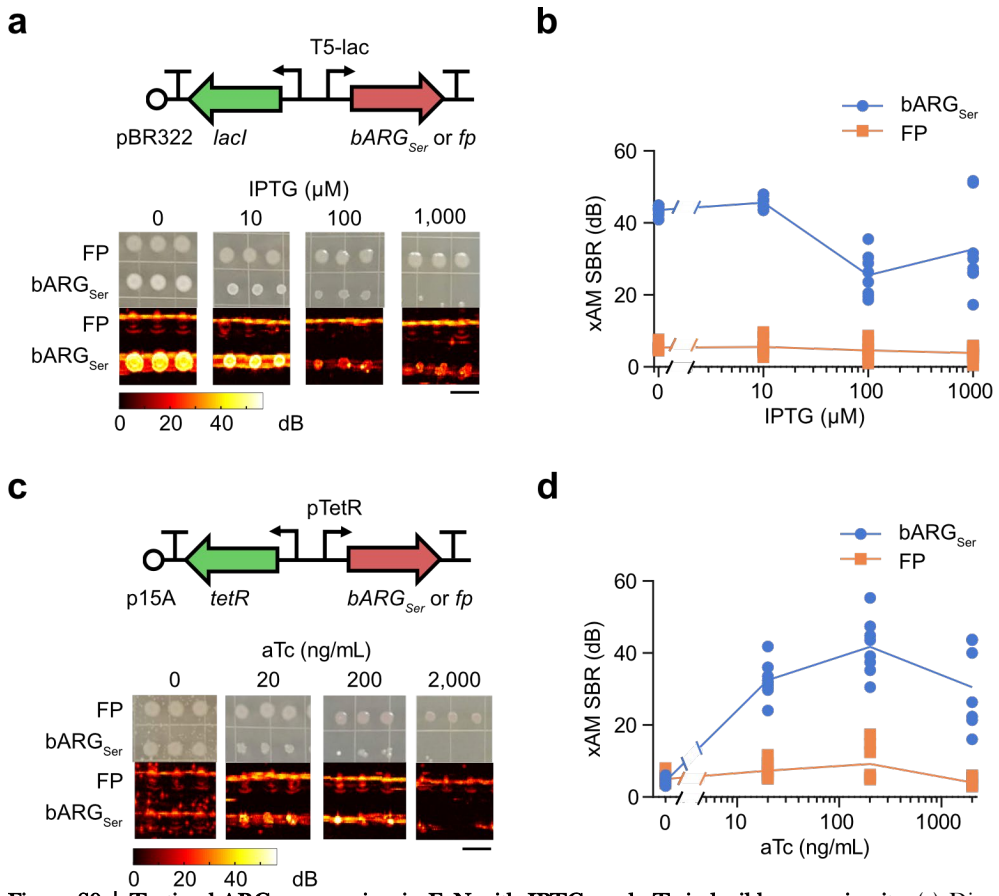

Figure S9 | Testing bARG$_{Ser}$ expression in EcN with IPTG- and aTc-inducible gene circuits. **(a)** Diagram of the IPTG-inducible construct used to express bARG$_{Ser}$ in EcN (top), and representative optical and xAM images of bARG$_{Ser}$-expressing or fluorescent protein (FP)-expressing patches of EcN on solid media with varying IPTG concentrations at 37°C (bottom). **(b)** Quantification of the xAM SBR of all patches from the experiment in (a) (n=8). **(c-d)** Same as in (a-b) but for the aTc-inducible construct. The scale bars in (a,c) represent 1 cm.

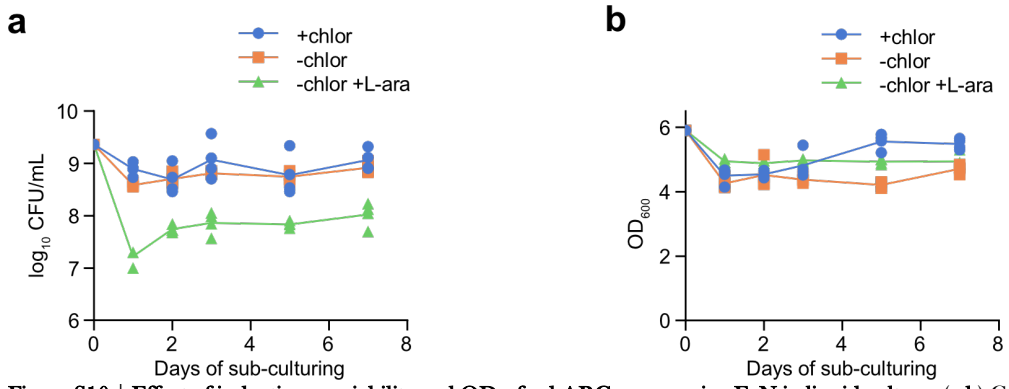

Figure S10 | Effect of induction on viability and OD_{600} for $bARG_{Sac}$-expressing EcN in liquid culture. (a-b) Colony forming units (CFU) per mL of culture (a) and optical density at 600 nm (b) during daily sub-culturing into LB media with 25 µg/mL chloramphenicol (+chlor), without chloramphenicol (-chlor), or without chloramphenicol and with 0.1% (w/v) L-arabinose (-chlor +L-ara) using pBAD-$bARG_{Sac}$-axetxe EcN.

a

		Non-white mutants / total colonies screened				
Condition	**Replicate**	**Starter**	**Day 1**	**Day 2**	**Day 3**	**Day 5**
+chlor	#1	0/226	0/68	0/69	0/60	0/40
+chlor	#2		0/55	0/47	0/355	0/54
+chlor	#3		0/48	0/39	0/98	0/42
+chlor	#4		0/56	0/21	0/49	0/233
-chlor	#1		0/39	0/54	0/70	0/64
-chlor	#2		0/28	0/46	0/65	0/46
-chlor	#3		0/47	0/57	0/75	0/52
-chlor	#4		0/36	0/57	0/57	0/38
-chlor +ara	#1		0/2	0/68	0/53	0/44
-chlor +ara	#2		0/2	0/62	2/86	0/68
-chlor +ara	#3		ND*	0/67	3/102	6/70
-chlor +ara	#4		0/1	0/76	0/34	0/56

*ND: no data because there were no colonies

b

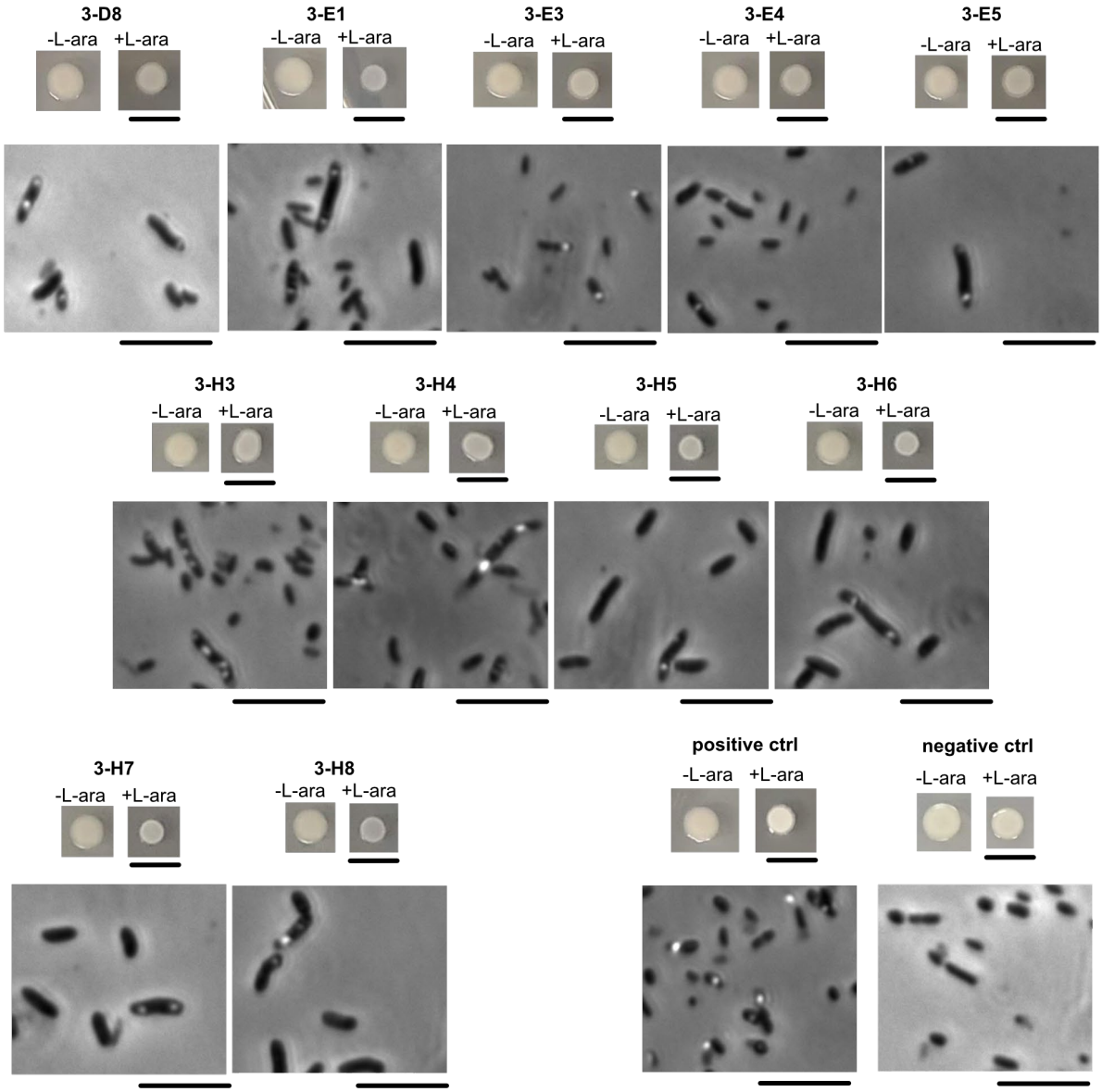

Figure S11 | Quantification and characterization of EcN mutants deficient in bARG$_{Ser}$ expression isolated from daily subculturing *in vitro*. (**a**) Numbers of non-white mutant colonies and total colonies screened on plates with 0.1% (w/v) L-arabinose from daily sub-culturing into LB media with 25 μg/mL chloramphenicol (+chlor), without chloramphenicol (-chlor), or without chloramphenicol and with 0.1% (w/v) L-arabinose (-chlor +L-ara) using pBAD-bARG$_{Ser}$-axetxe EcN. Cultures where mutants were found are indicated in red. (**b**) Optical images of patches (top rows) on fresh plates with 0.1% (w/v) L-arabinose (+L-ara) and without L-arabinose (-L-ara), and phase contrast microscopy images (bottom rows) from the 11 mutant colonies in (a). Mutants 3-D3 and 3-E1 were from the culture -chlor +ara, replicate #2, day 3; mutants 3-E3, 3-E4, and 3-E5 were from the culture -chlor +ara, replicate #3, day 3; and mutants 3-H3 through 3-H8 were from the culture -chlor +ara, replicate #3, day 5. The positive and negative controls were wild-type pBAD-bARG$_{Ser}$-axetxe EcN and pBAD-FP-axetxe EcN, respectively. Scale bars are 1 cm for images of patches and 10 μm for microscopy images.

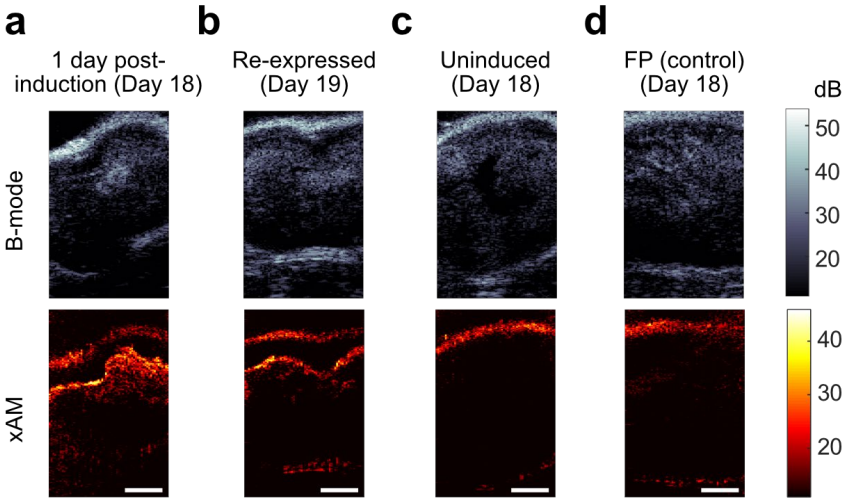

Figure S12 | xAM ultrasound imaging of mouse tumors colonized by EcN. (**a-c**) Representative B-mode (top, grayscale) and xAM (bottom, hot-scale) ultrasound images of tumors colonized by pBAD-bARG$_{Sc}$-axetxe EcN at least 24 hours after induction with L-arabinose on day 18 (a), at least 24 hours after collapse and re-induction (day 19) (b), or uninduced on day 18 (c). (**d**) Representative ultrasound images of tumors colonized by pBAD-FP-axetxe EcN at least 24 hours after induction with L-arabinose on day 18. Scale bars in (a-d) represent 2 mm. See **Fig. 4a** for the corresponding *in vivo* protocol and **Fig. 4j** for the quantification of the xAM SBR for these images.

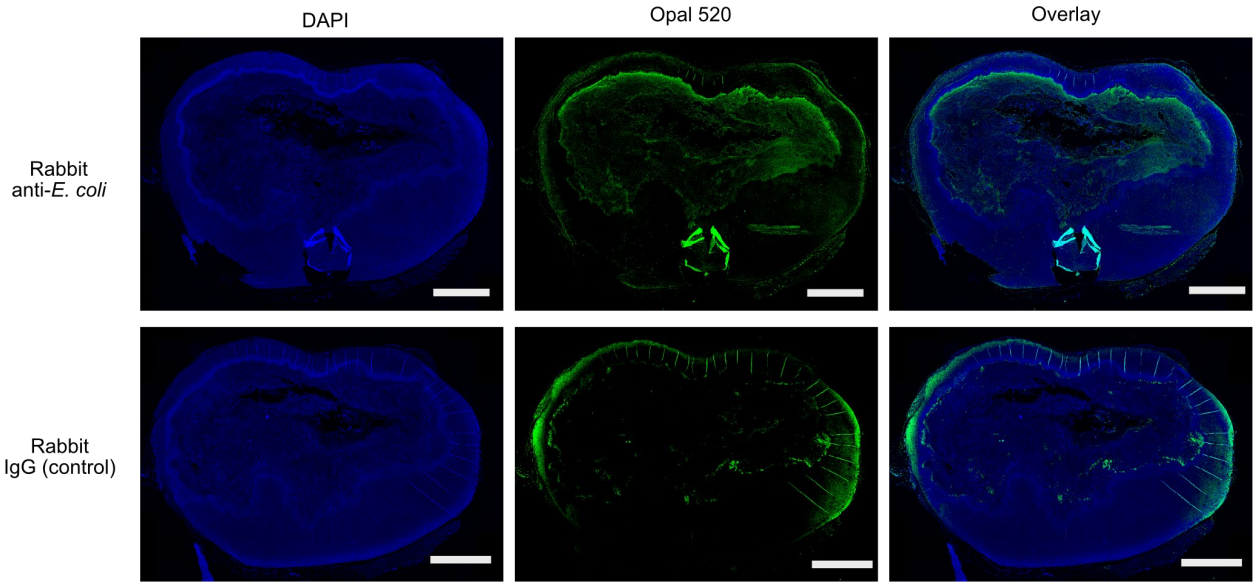

Figure S13 | Histology of MC26 tumor colonized with bARG$_{Sw}$-expressing EcN. Fluorescent images of tissue sections after ultrasound imaging on day 19 (see **Fig. 4a**). Sections were incubated with either polyclonal rabbit anti-*E. coli* antibodies (top row) or non-reactive rabbit IgG isotype control antibody (bottom row) as a negative control. All sections were then incubated with an Opal 520 polymer anti-rabbit HRP antibody (Akoya biosciences) and counterstained with DAPI. The EcN are visible in the necrotic core in the Opal 520 channel (top middle panel); the edges of the tissue exhibit a high degree of background staining (bottom middle panel).

a

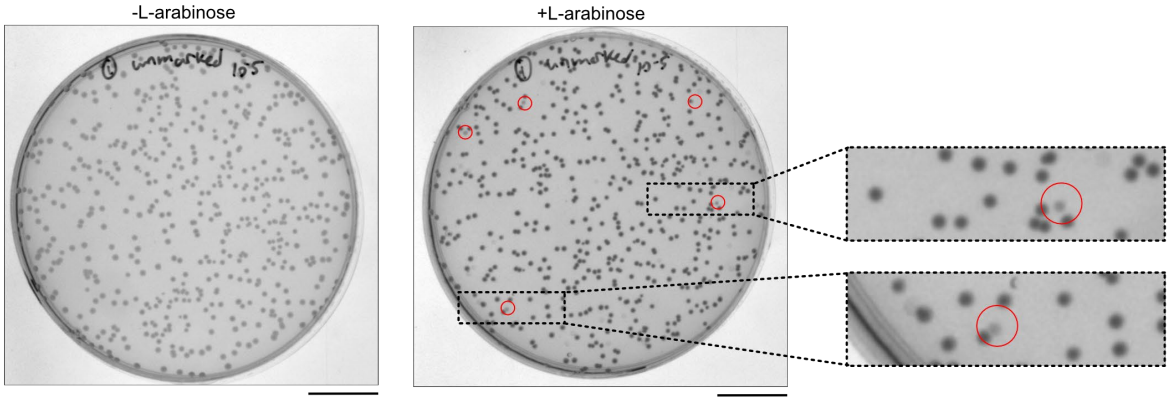

b

Mouse	Condition	Non-white mutants / total colonies screened
#1	Induced	0/687
#2	Induced	2/807
#3	Induced	0/341
#4	Induced	0/478
#5	Induced	5/585
#6	Uninduced	0/660
#7	Uninduced	0/567
#8	Uninduced	0/553
#9	Uninduced	0/556
#10	Uninduced	0/863
Total		7/6097 ~ 0.1%

c

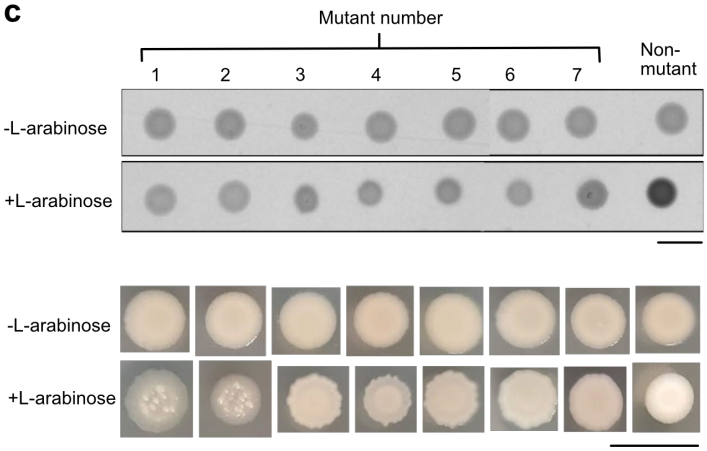

Figure S14 | Screening for EcN mutants defective in bARG$_{Sc}$ expression isolated from colonized tumors. (**a**) White light transmission images of plates with 0.1% (w/v) L-arabinose and without L-arabinose from plating a tumor (from mouse #5 in (b)) colonized by bARG$_{Sc}$-expressing EcN. Mutant colonies on the +L-arabinose plate appear lighter (more translucent) than wild-type opaque colonies and are indicated by red circles. (**b**) Numbers of non-white mutant colonies and total colonies screened on plates with 0.1% (w/v) L-arabinose for the ten mice injected with pBAD-bARG$_{Sc}$-axetxe EcN. **c**, White light transmission images (top) and photographs (bottom) of patches on fresh plates with 0.1% (w/v) L-arabinose and without L-arabinose made from the seven translucent mutant colonies in red in (b) and an opaque non-mutant colony as a control. Mutants 1-2 were from mouse #2 and mutants 3-7 were from mouse #5. Scale bars are 2 cm in (a) and 1 cm in (c).